Università degli Studi di Urbino Carlo Bo

Department of Pure and Applied Sciences

Ph.D. COURSE IN: Basic Sciences and Applications

CURRICULUM: Earth Sciences

SERIES: XXXIII

Thermal Structure and Active Tectonics of the Frontal Zone of the Zagros Fold and Thrust Belt in Western Lurestan, Iran: New Insights from 3-D Geothermal Analytical Modelling and 2-D Structural Finite Element Modelling

Academic discipline: GEO/10 – Solid Earth Geophysics

SUPERVISORS:
Prof. Stefano Santini
Prof. Stefano Mazzoli

CO-SUPERVISOR:
Ph.D. Antonella Megna

Ph.D. student: Matteo Basilici

ACADEMIC YEAR 2019-2020

Table of contents

1 – Introduction

In the last century several authors tried to understand the geological and geophysical setting of the Zagros mountain chain. The result of these studies pointed out a mesozoic continental-continental collision between Eurasia and Arabia plates due to the closure of the Neo-Tethys ocean (Alavi, 1994, 2007; Agard et al., 2005; Berberian and King, 1981; Dercourt et al., 1986; Mouthereau et al., 2012; Stampfli and Borel, 2002; Vergés et al., 2011a). At the present, the orogenic process is still active, as confirmed by recent geodetic calculation provided by Vernant et al. (2004). It indicates a motion of the Arabian plate relative to fixed Eurasia of ~ 20 mm/yr, this is partitioned between right-lateral motion along NE-SW-Striking faults and NW-SE thrusts front (Blanc et al., 2003; Vernant et al., 2004; Talebian and Jackson, 2002). The working area of this thesis is localized in the northern part of the Zagros orogen i.e. Lurestan arc (Figure 1). In this sector of the Zagros orogen a master blind fault known as Mountain Front Fault and named here Main Frontal Thrust nucleated a large earthquake (Mw = 7.3) in November 12, 2017 highlighting the deep structure of this sector of the Zagros Mountain chain (Basilici et al. 2020b; Gombert et al., 2019; Nissen et al., 2019; Tavani et al., 2018a; Wang et al., 2018).

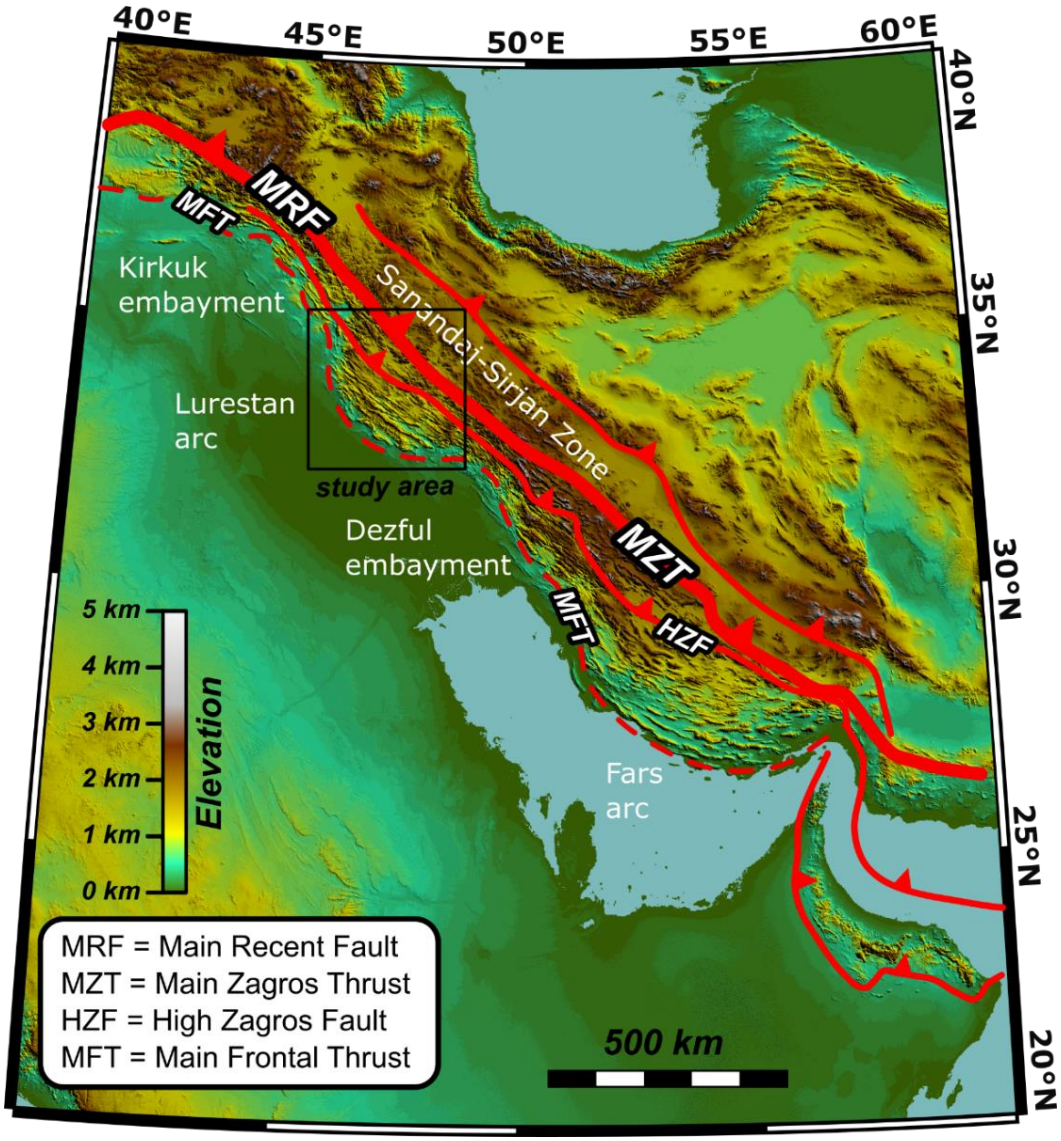

Figure 1 – Tectonic sketch map of the Zagros mountain belt (modified from Basilici et al. 2020a).

The aim of this thesis is to explain how the Main Frontal Thrust interacts with the entire Lurestan arc in terms of thermal structure and active deformation. To reach the prefixed scope we used a mathematical approach studying the major thrust fault by analytical and numerical procedures in order to realize exhaustive 2-D and 3-D models.

We present here the 3-D model of the Lurestan arc thermal structure calculated using an analytical procedure interpolated with polynomial equations. The model took into account topography, sedimentary cover, basement, thrusts and Moho depth constrained by the physical properties of the rocks as thermal conductivity and heat production rate (Basilici et al., 2019; 2020a).

To study the active deformation, instead, we realized a 2-D model of co-seismic and inter-seismic deformation of the Main Frontal Thrust applying the finite element modelling methodology performed here using Marc Software (MSC Software Corporation). In this case we set a pre-built model that was divided into several domains, to which average values of Young's modulus, Poisson's ratio and density was assigned. To resolve the system, the entire model was discretized into an equivalent assemblage of small structures (elementary component, named mesh). As a result, for each unit, a solution was formulated and combined to obtain the solution for the entire system (Basilici et al., 2020b). The boundary condition was set up based on available GPS dataset (Vernant et al., 2004).

Both 3-D thermal structure model and 2-D active deformation FEM model were calculated on a geological model describing the main Lurestan arc crustal structures. The geometry of the tectonic features was built on the base of previous published geological cross section (Tavani et al., 2018a; 2020; Vergés et al., 2011a). At the end, we compared the obtained thermal structure with previous studies and the active deformation model with an investigation of a large-scale features of topography.

2 – Geological and Seismological Background

2.1 – Geodynamic Evolution

The first recognizable tectonic event in the study area occurred at the end of the Carboniferous period, with the onset of the Variscan orogeny. Prior to this time, the entire region was a stable continental platform. Paleomagnetic poles indicate that Iran remained close to Arabia during at least the early part of the Permian, to detach itself subsequently, at the end of the same period (Berberian and King, 1981).

The entire Mesozoic represented the era in which the High-Zagros Alpine Ocean in the southern region of Iran closed, during this time the Arabian foreland was subjected to progressive subsidence and normal faults parallel to the old continental margin was formed, these extensional movement was linked to the opening (occurred at that time) of the Neo-Tethys ocean (Jassim and Goff, 2006; Berberian and King, 1981).

A phase of rifting occurred from the Early to the Late Jurassic time (Pratt and Smewing, 1990). The extensional deformation is testified by syn-sedimentary faults, block tilting, unconformities and by facies and thickness change (Tavani et al. 2018a; 2018b) that produced a strong control on the structure of the present mountain belt (Bahroudi and Talbot, 2006; Jackson and Fitch, 1981; Tavani et al., 2020). Schettino and Scotese (2002) suggested that the mechanism of this rifting phase was due to a tensional force related to the north easterly subduction of the old Neo-Tethys oceanic lithosphere beneath the active margin of Eurasia extending from the northern Turkey to the Sanandaj-Sirjan Zone of Iran.

Another phase of oceanic floor spreading around the northern margin of the Arabian Plate is marked by an important regional unconformity related to Mid Tithonian which marks the boundary between Megasequences AP7 and AP8 (Sharland et al., 2001). The oceanic floor spreading continued during Early Cretaceous until Late

Cretaceous in which the south-eastern oceanic crust was abducted onto the Arabian Plate, it formed the ophiolite succession actually representing the Neo-Tethys ocean remainder (Figure 2), In Early Campanian a pulse of compression formed a foreland basin around the northern margin of the Arabian Plate (Warburton et al., 1990) and the oceanic lithosphere of the southern Neo-Tethys are interpreted to have been subducted into the southern subduction zone (Searle et al. 2004). Also during this time, pre-abducted ophiolites were metamorphosed and finally involved into the Zagros suture zone during late Miocene (Jassim and Goff, 2006; Leterrier, 1985).

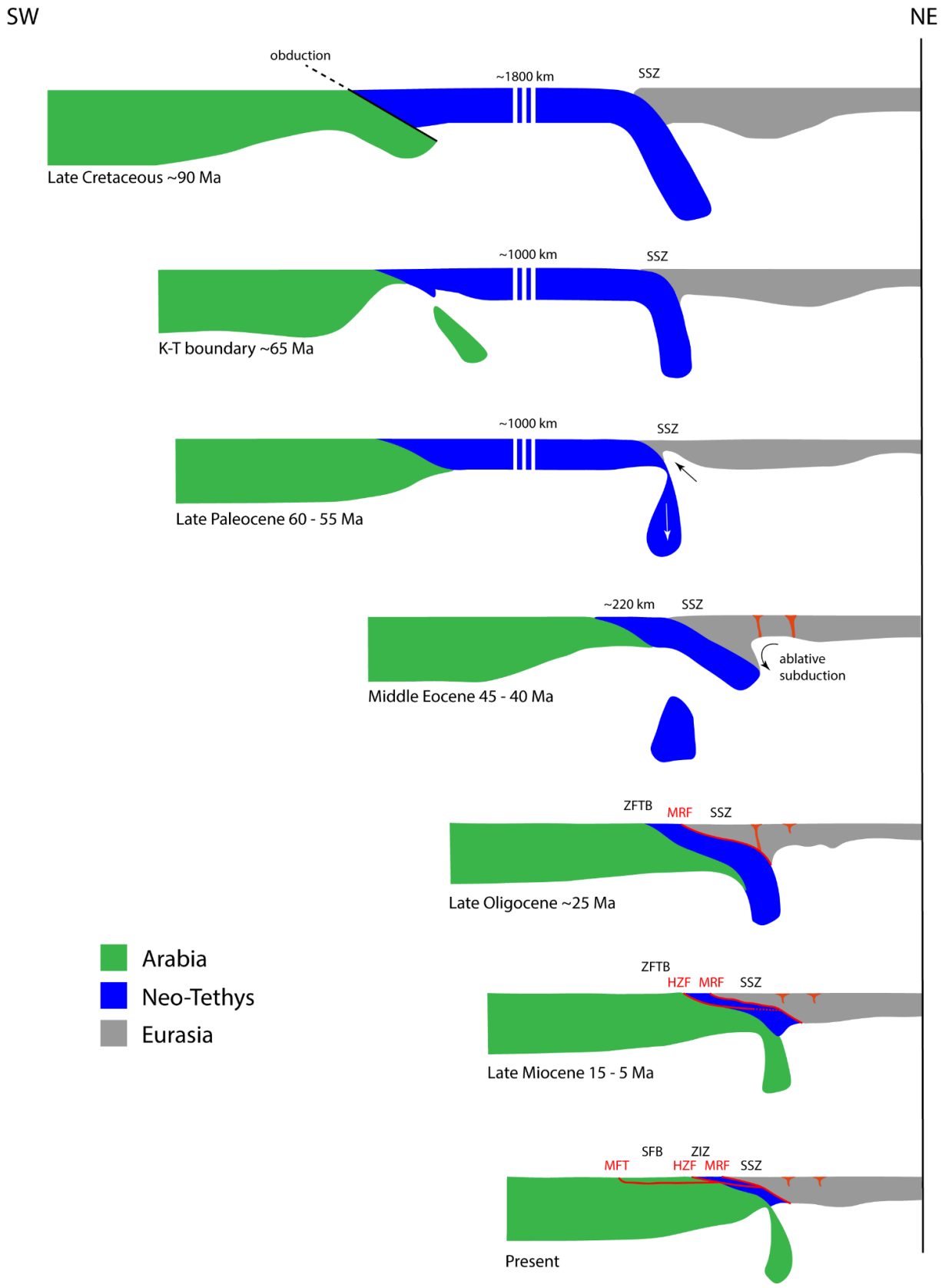

Figure 2 – Sketch of the geodynamic evolution of the Lurestan arc from Late Cretaceous to Present (modified from Agard et al., 2011). Abbreviations: SSZ – Sanandaj-Sirjan Zone; ZFTB – Zagros Fold and Thrust belt; SFB – Simply Folded Belt; ZIZ – Zagros Imbricated Zone; MRF – Main recent Fault; HZF – High Zagros Fault; MFT – Main Frontal Thrust.

Evidence of subduction and the final closure of the Neo-Tethys ocean are attributable to Paleocene-Eocene (Ghasemi and Talbot, 2006; Mouthereau et al. 2012). In late Eocene (~35 Ma) further compressional event occurred driven by the distal continental margin negative buoyancy, resulting in the effective continent-continent collision between Eurasia and Arabia during Oligocene (~25 Ma) (Agard et al. 2005; Gavillot et al., 2010; Mouthereau et al. 2012).

The temporal evolution of the Zagros topography and adjacent Iranian plateau uplift scarcely well understood but it is generally believed that the subsequent growth of the large Zagros anticlines occurred during Miocene (~15 - 12 Ma; Mouthereau et al. 2012) to continue during Plio-Pleistocene in the Zagros Fold and Thrust belt (Hessami et al. 2001). The presence of dextral strike-slip dominated and reverse dominated domains within the Kurdistan area indicates that an oblique convergence guides the entire history of the Zagros orogeny since the Late Cretaceous obduction of the Neo-Tethys oceanic realm (Allen et al., 2011; Sadeghi and Yassaghi, 2016).

Currently it is believed that convergence slowed down by ~30% from ~5 Ma to present day (Austermann and Iaffaldano, 2013). On the contrary, from ~5 Ma the Zagros Fold and Thrust belt in the Kurdistan region experienced major basement-involved thrusting, (Allen et al., 2004; Austermann and Iaffaldano, 2013; Mouthereau, 2012; Koshnaw et al., 2017). During this recent period the shortening in the northern part of the Zagros Fold and Thrust belt was ~49 km (Blanc et al., 2003) with an active deformation rate of ~10 mm/yr (Allen et al., 2004), but a qualitative analysis of striated fault planes suggests a variable shortening direction along the strike of the mountain belt. However, shear sense indicators from thrust surfaces in various parts of the mountain belt reveal a dominant SW direction of transport (Alavi, 2007; Csontos et al., 2012; Hessami et al., 2006).

The last geodetic calculation was performed in 1999 September and 2001 October, it confirmed a northward motion of the Arabian plate of ~20 mm/yr in the fixed-Eurasia reference frame (Vernant et al., 2004). The Iran block is actually considered as a microplate located in between the Arabian plate and the Eurasian plate

in sensu stricto (Alavi, 1994; 2007; Berberian and Berberian, 1981; Colman-sadd, 1978; Stocklin, 1968).

2.2 – Tectonic Setting and Crustal Structures

The Lurestan arc is part of the so-called Zagros Fold and Thrust belt (ZFTB). It comprises the Simply Folded Belt (SFB) and the Zagros Imbricated Zone (ZIZ; Figure 3). The SFB constitutes the external and less-strained part of the active Zagros orogen wedge, bounded from the ZIZ to the north-east by the High Zagros Fault (HZF). The suture zone between the ZIZ of the Arabian Plate and the Sanandaj-Sirjan Zone (SSZ) of the Iran block is represented by the Main Recent Fault (MRF; Alavi, 1994; Berberian, 1995). An important feature of the Arabian plate margin is the coexistence of thin-skinned and thick-skinned settings (Le Garzic et al., 2019; Nissen et al., 2011; Tavani et al., 2018a; 2018b).

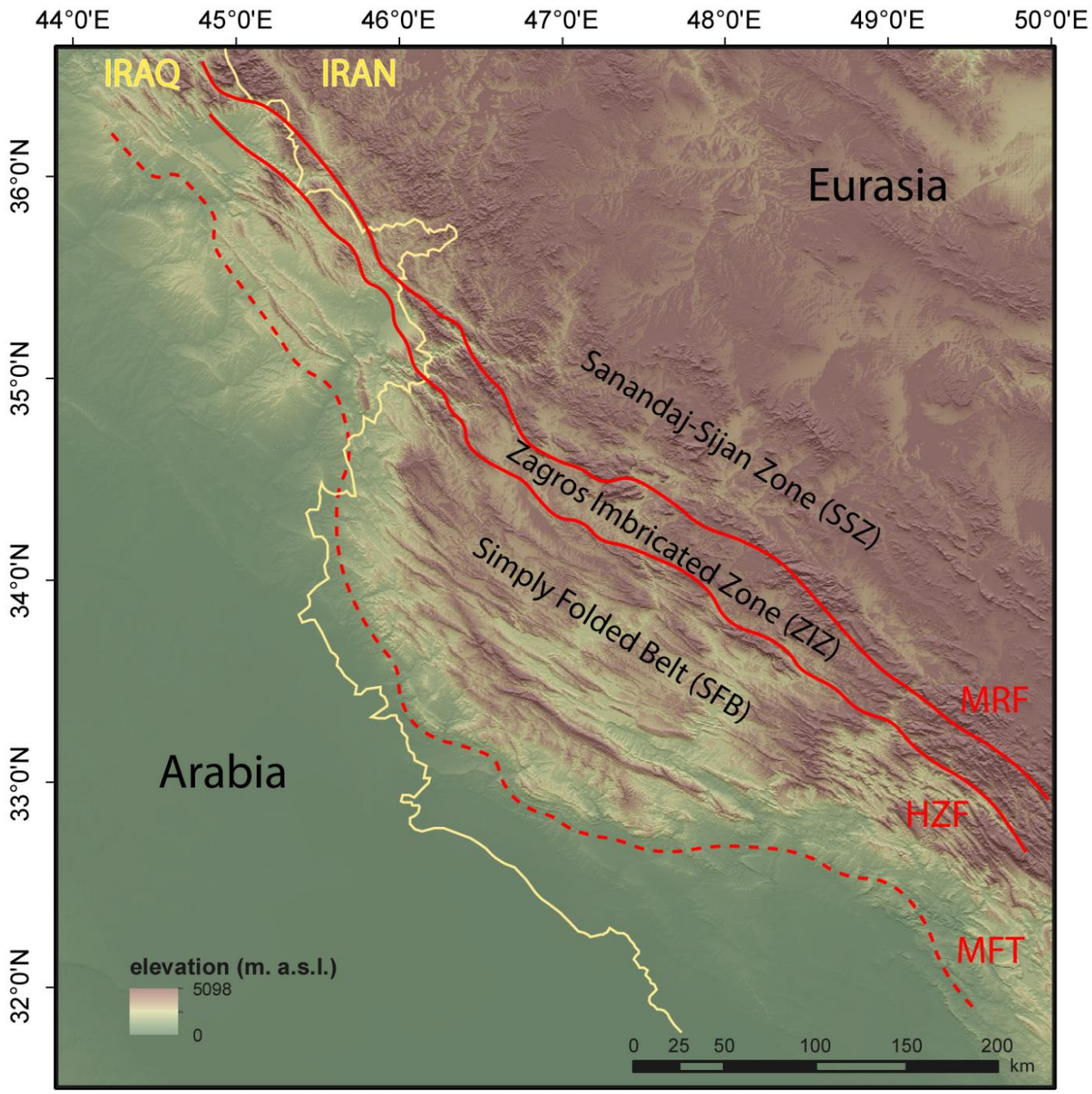

Figure 3 – Sketch map of the Lurestan arc tectonic setting. The yellow line represents the political boundary between Iraq and Iran. Red lines are the traces of Main Recent Fault (MRF) and High Zagros Fault (HZF). The red dashed line is the trace of Main Frontal Thrust (MFT).

The MRF is the most studied fault of the entire mountain chain. It is the major seismically active right-lateral strike-slip fault and it is structurally distinct along its entire length (Berberian, 1995). Based on the drainage pattern restoration, the offset of the MRF may be as much as 70 km geometrically linked to a shortening of ~50 km which is a substantial fraction of the 85 – 140 km total Arabia – Eurasia convergence over the last 3 – 5 Ma. The calculated horizontal slip rate on the MRF would then be

in the range of 10 – 17 mm/yr, with a vertical component of 0.1 – 0.2 mm/yr (Authemayou et al. 2006; Talebian and Jackson, 2002). Using a FEM model, Vernant and Chéry (2006) calculated a strike-slip fault accommodation of ~25% of the total lateral shear strain, the remaining ~75% could occur in the orogen itself by a more distributed deformation.

The High Zagros Fault (HZF) is a reverse fault with a vertical displacement more than 6 km. Uplift is ongoing since the Early Miocene. In the south-eastern Zagros this fault reaches the Mountain Front Flexure (MFF) and it was associated with several earthquakes with $M_w \geq 5$ (Berberian, 1995).

The Mountain Front Flexure (MFF; Falcon, 1961) named here Main Frontal Thrust (MFT, Basilici et al. 2020a; 2020b) represents the major thrust structure and, therefore, the main topic of this thesis. It is a large basement blind fault showing the typical ramp-flat geometry of more than 1350 km long and a max value of 9.7 km of cumulative displacement. It accommodated most of the shortening (Hessami et al., 2006) and it has important structural, topographic, geomorphic and seismotectonic characteristics (Berberian, 1995; Emami et al., 2010; Koshnaw et al., 2017; Sherkati et al., 2006; Tavani et al., 2018a). Topographical and geophysical evidences suggest that, in the Lurestan arc, the MFT developed at 8.1 – 7.2 Ma (Homke et al., 2004; Koshnaw et al., 2017). Tavani et al. (2020) suggest that it nucleates in the inner portion of the necking domain of the Jurassic rift, where the mid-crustal ductile level is sufficiently thick to promote the development of a large and interconnected decollement, from which the MFT emanates.

The most north-eastward topographic expression of the MZT is represented by the Anaran anticline which is also the most recent (1.5 Ma) and external fold of the Zagros orogen (Emami et al., 2010). It was interpreted by Vergés et al. (2009; 2011a) as forming part of the multi-detachment fold system of the Lurestan arc governed by the varying mechanical stratigraphy. The sinusoidal shape of the MFT and its different position in the Kirkuk embayment and Lurestan arc was promoted by lateral segmentation of the Jurassic rift accommodated by transfer faults (Tavani et al., 2020)

and it is probably that in this boundary area (Lurestan arc – Kirkuk embayment) the deep faulting is decoupled by the shallow folding (Nissen et al., 2019). The main seismic events of the ZFTB are largely nucleated by this thrust fault (Talebian and Jackson, 2004). Recently, earthquake magnitude reached high values as testified by events of November 12, 2017 (M_w = 7.3; Tavani et al., 2018a) and November 25, 2018 (M_w = 6.3).

Several authors investigated the thickness of the crust of the Iran sector using different techniques. On this thesis we took into account only those work where the Lurestan sector is comprised.

Paul et al. (2006; 2010) calculated a Moho depth comprises in the range of 40 - 55 km for the Lurestan arc using two temporary passive seismic experiment across the central and northern Zagros. Jiménez-Munt et al. (2012) produced the first 3-D model of the crustal geometry calculated from the geoid height and elevation data combined with thermal analysis, confirming previous studies (Paul et al., 2006; 2010) and tightening the Lurestan arc Moho depth in a range of 44 – 52 km. All results obtained by previous authors were combined and used in Tunini et al. (2015) to produce a numerical 2-D model of the thermal, compositional, density and seismological structure of the crust and upper mantle along two transect across the entire Arabia-Eurasia collision zone. A recent 2-D model of the sedimentary cover-basement interface and Moho depth was performed by Teknik et al. (2019) coincident with a CIGSIP (China-Iran Geological and Geophysical Survey in the Iranian plateau) seismic profile. Therefore, the results are constrained mainly by a receiver function seismic section, but also by published highest resolution data about crustal Iranian geophysics available at present. Today new Moho depth investigation techniques are improving, as the Moho estimation from GOCE Gravity Data (Heydarizadeh-Shali et al., 2020) and phase velocity ambient noise tomography (Movaghari and Javan-Doloei, 2019) confirming, in Iran, the results of previous authors.

2.3 – Stratigraphy

The characteristic collision zone of the Zagros mountain chain is constituted by two main domains belonging to Arabian plate and Iran block respectively. ZFTB formed by the typical sedimentary succession of the Arabian margin (Figure 4), resting on top of a Pre-Cambrian crystalline basement which does not take part in the typical shallower folding, the basement-cover interface is therefore a decollement level (Alavi, 2007; Blanc et al., 2003; Casciello et al., 2009; Colman-sadd, 1978; Emami et al., 2010; Hessami et al., 2001; Massaro et al., 2019; Sepehr and Cosgrove, 2004; Vergés et al., 2011a). Probably the Lurestan arc does not present the Hormuz salt, a sequence of evaporites that were deposited during Early Cambrian and located instead, on the Fars arc (Talbot and Alavi 1996; Vergés et al., 2011a; 2011b). Teknik and Ghods (2017) and Teknik et al. (2019) calculated the total thickness of the Arabian Cover using a fractal spectral method to the aeromagnetic map of Iran and a gravity magnetic modelling respectively. The result is an Arabian Cover thickness of the Lurestan arc comprised between 6 and 16 km. Therefore the basement is not exposed in the ZFTB and the nearest exposures are mapped in central Iran (Saghand Area; Ramezani, 1997; Ramezani and Tucker, 2003).

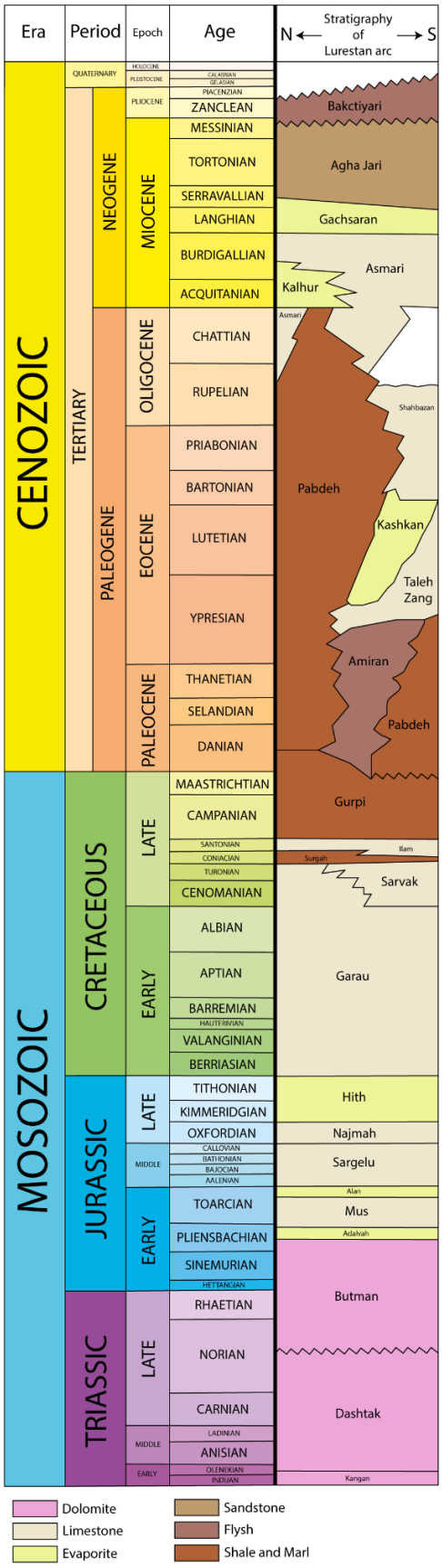

Figure 4 – Mesozoic-Cenozoic stratigraphy of the Lurestan arc sedimentary cover (modified from Beydoun et al., 1992; Jassim and Goff, 2006; Motiei, 1993; Sepher and Cosgrove, 2004).

The ZIZ is a more stratigraphic complex zone, it is the core of the orogen where the intensity of deformation has reached its maximum. It presents the remainder of the Neo-Tethys ocean obducted in an ophiolitic succession (Figure 2), a Radiolarite Zone and a series of magmatic units (Alavi, 2007; Agard et al., 2005; Berberian and King, 1981; Dercourt et al., 1986; Ghasemi and Talbot, 2006; Leterrier 1985; Sadeghi and Yassaghi, 2016; Vergés et al., 2011a).

The Sanandaj-Sirjan Zone (Iran Block) is formed mainly by methamorphic rocks, by Jurassic to Early Eocene calk-alkaline magmatic rocks, and by the products of Middle Eocene gabbroic plutonism (Alavi, 1994; Baharifard et al., 2004; Berberian and Berberian, 1981; Leterrier, 1985).

2.4 – Seismicity

The present seismicity of the Zagros orogen is studied from late ‘60s (e.g. Falcon, 1969; Dewey and Grantz; 1973) and it covers the entire width of the Lurestan arc. Berberian (1976) produced the first seismotectonic map of Iran. Today, earthquake data from 1967 are available on Global CTM and USGS catalogues (Figure 5).

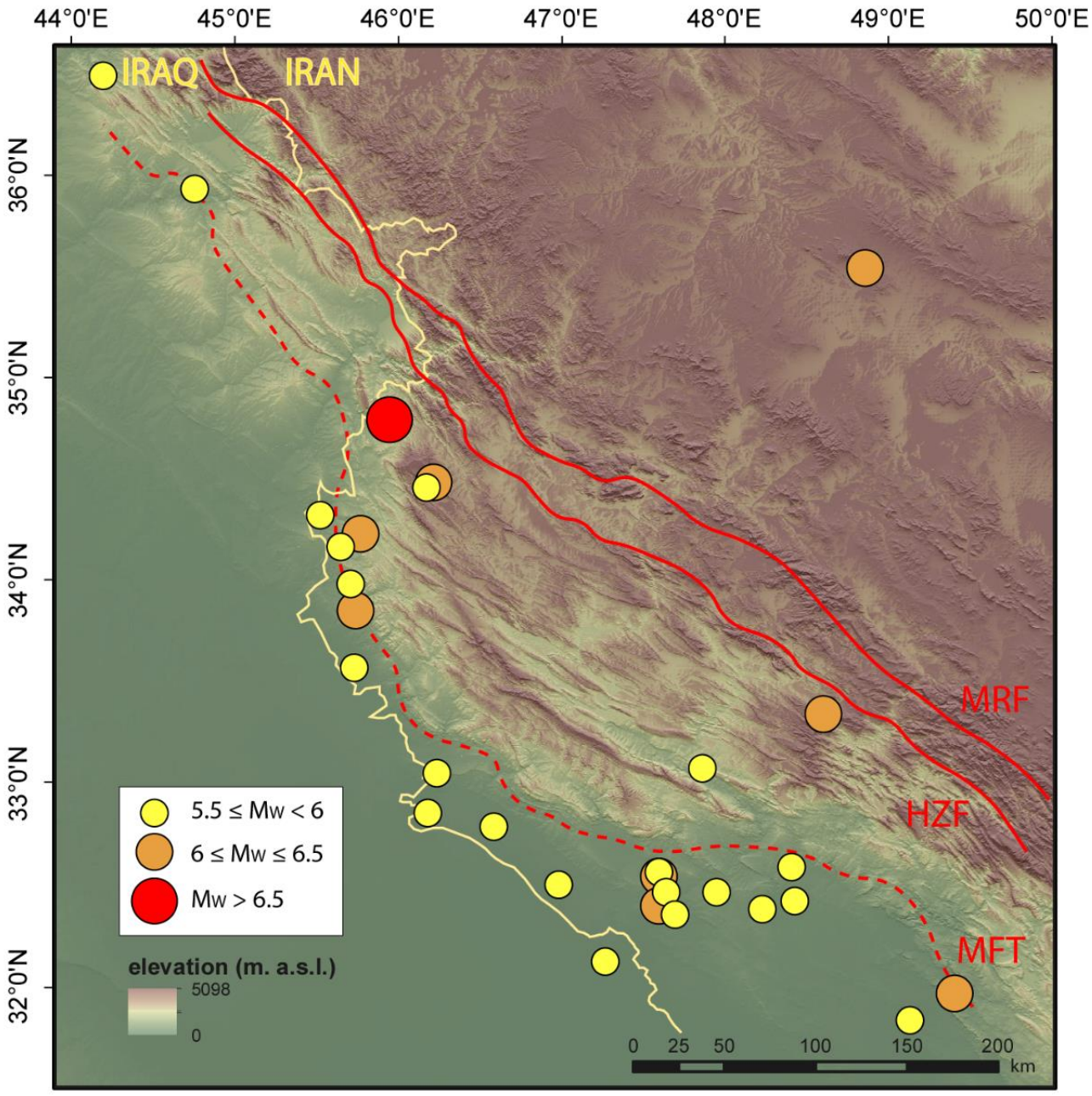

Figure 5 – Earthquake with Mw ≥ 5.5 recorded from 1967 to the present day in Lurestan arc. The red dot is the main seismic event of November 12, 2017 (Mw = 7.3). The data are from the USGS catalogue (https://earthquake.usgs.gov/earthquakes/search/; last access: 04 May 2020).

There are two distinct types of seismic active fault plane solution in the Lurestan arc, a dextral strike-slip NW-SE striking faults and reverse faults respectively (Allen et al., 2011; Authemayou et al., 2006; Basilici et al. 2020a; Talbot and Alavi, 1996; Talebian and Jackson 2002). The strike-slip faulting nucleates seismic events with increasing magnitude going from SW into the SFB, where the reverse faulting is

dominating, to NE in proximity of the MRF. Here the magnitude of strike-slip fault nucleated earthquakes reaches its maximum (Mw ~ 5; Talebian and Jackson, 2002). The seismicity confirmed the study of Vernant and Chery (2006) in which they calculated an accommodation of ~25% of the total lateral shear strain carried by the MRF.

The reverse faulting comprises minor shallow reverse faults and deep thrusts localized into the basement (Hessami et al., 2006; Jackson, 1980; Jackson and Fitch, 1981), the master blind thrust, named here MFT, can generate large earthquakes (Berberian, 1995) as confirmed by November 12, 2017 (Mw = 7.3) seismic event nucleated at depth of ~19 km (Basilici et al. 2020a; Gombert et al., 2019; Nissen et al., 2019; Tavani et al., 2018a; Wang et al., 2018). Therefore, the totality of the seismicity (seismogenetic level) occurs into the crust or upper lithospheric mantle (depth range of 5 – 35 km). There are not recorded earthquakes into the deep mantle below the ZFTB (Engdahl et al., 2006). This particularity of the Arabia-Eurasia collision zone made the authors understand that the subduction of the Arabian plate below the Eurasian plate is inactive at present and the slab put in place a break off (Austermann and Iaffaldano, 2013; Monthereau et al., 2012).

3 – 2-D and 3-D Geological Models

3.1 – Dataset

To improve analytical and numerical calculations in the Lurestan arc, a geological model of the area is requested as a base for mathematical procedures. For this purpose, we used the published balanced cross sections located on the study area. In Figure 6 we show geological cross sections located on the Lurestan arc and used to build 2-D and 3-D geological models. In each geological cross sections (shown in Figures 7, 8 and 9) the entire sedimentary succession was unified in a unique geological unit i.e. Arabian sedimentary cover, resting on top of the crystalline basement (Basilici et al., 2019; 2020a; 2020b).

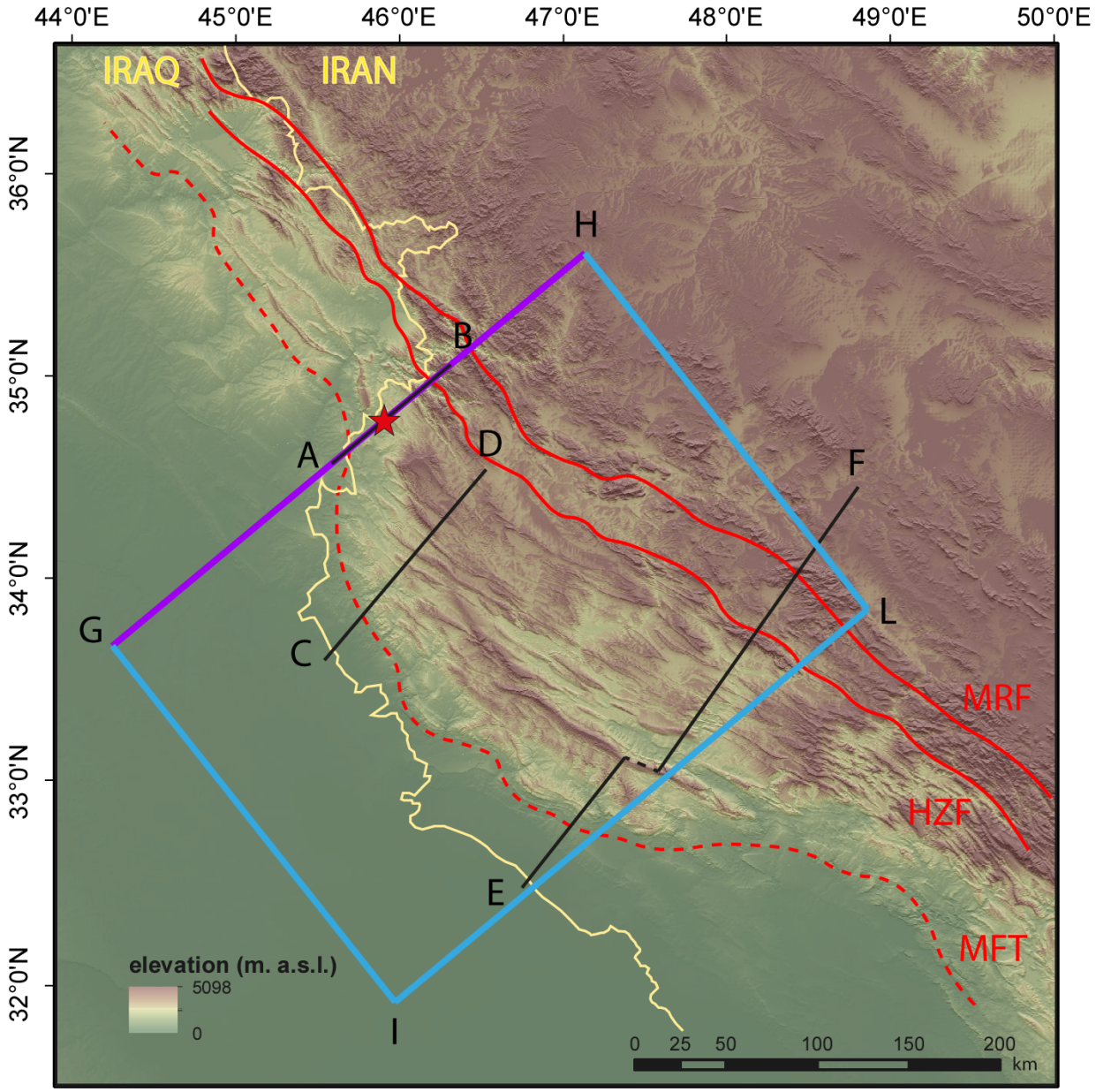

Figure 6 – Tectonic sketch map of the Zagros mountain belt. The yellow line represents the political boundary between Iraq and Iran. Red lines are the traces of the Main Recent Fault (MRF) and the High Zagros Fault (HZF). The red dashed line is the trace of the Main Frontal Thrust (MFT). The black segments AB, CD and EF are the cross sections by Tavani et al. (2018a; 2020) and Vergés et al. (2011a) respectively and shown in Figures 7, 8 and 9. The violet line GH is the 2-D geological model shown in Figure 10. The blue rectangle is the area of the 3-D geological model shown in Figure 12. Red star is the epicentral position of the main seismic event of 12 November 2017 (Mw = 7.3; Tavani et al., 2018a).

In Figure 7 is shown the balanced geological cross section (AB segment of Figure 6) by Tavani et al. (2018a). It based on geological observation, interpretation of seismic reflection profiles and well data, and crosses the epicentral area of 12 November 2017 earthquake (Mw = 7.3) so providing a comprehensive picture of the MFT geometry.

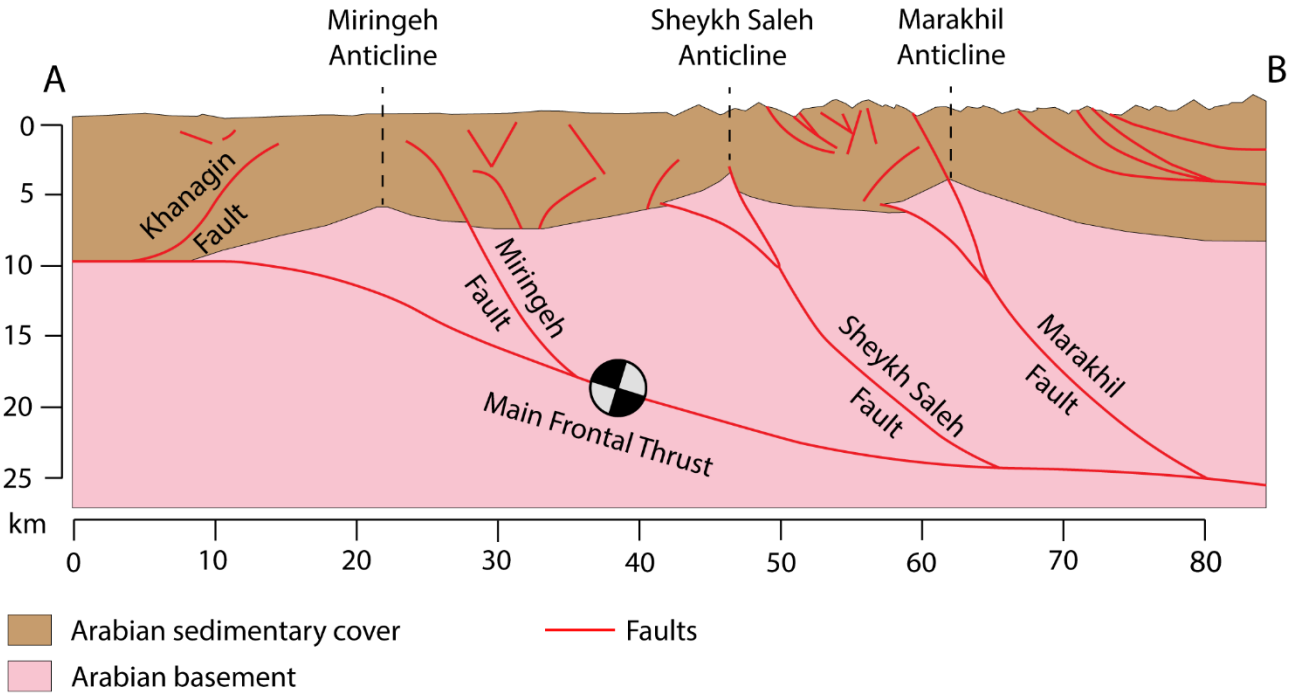

Figure 7 – Published geological cross section by Tavani et al. (2018a), AB segment in Figure 6. The entire sedimentary cover was unified in a unique unit (Basilici et al., 2019; 2020a; 2020b) The focal mechanism is projected in section and it shows the hypocentre of the 12 November 2017 earthquake (Mw = 7.3).

In Figure 8 is shown the balanced geological cross section (CD segment of Figure 6) by Tavani et al. (2020). It based on geological observation, geomorphic analysis, interpretation of seismic reflection profiles and earthquake data. It provides to highlight the thick-skinned structural setting of the Lurestan arc central part.

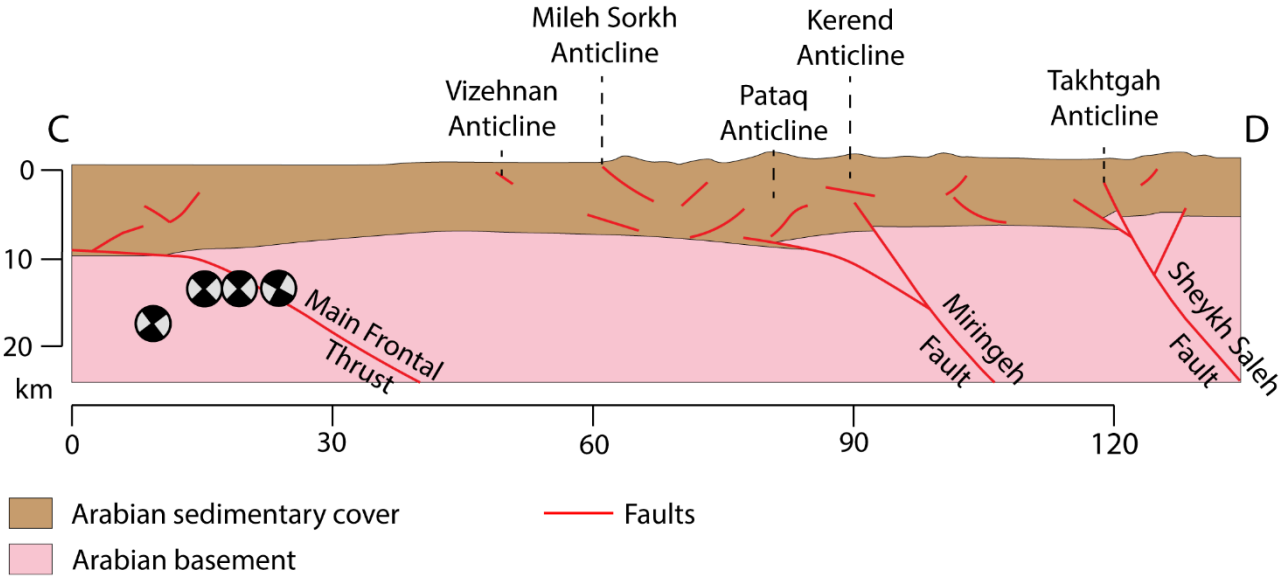

Figure 8 – Published geological cross section by Tavani et al. (2020), CD segment in Figure 6. The entire sedimentary cover was unified in a unique unit (Basilici et al., 2019; 2020a; 2020b). Focal mechanisms are projected in section and show the hypocentres of Mw > 5 earthquakes associated with the aftershock sequence of the 12 November 2017 earthquake (Mw = 7.3; Figure 7).

In Figure 9 the balanced geological cross section is shown, (EF segment of Figure 6) as provided by Vergés et al. (2011a). Paul et al. (2010) constrained the Moho depth using seismic receiver functions and seismic tomography sections. It provides to highlight the deepest part of the Lurestan arc.

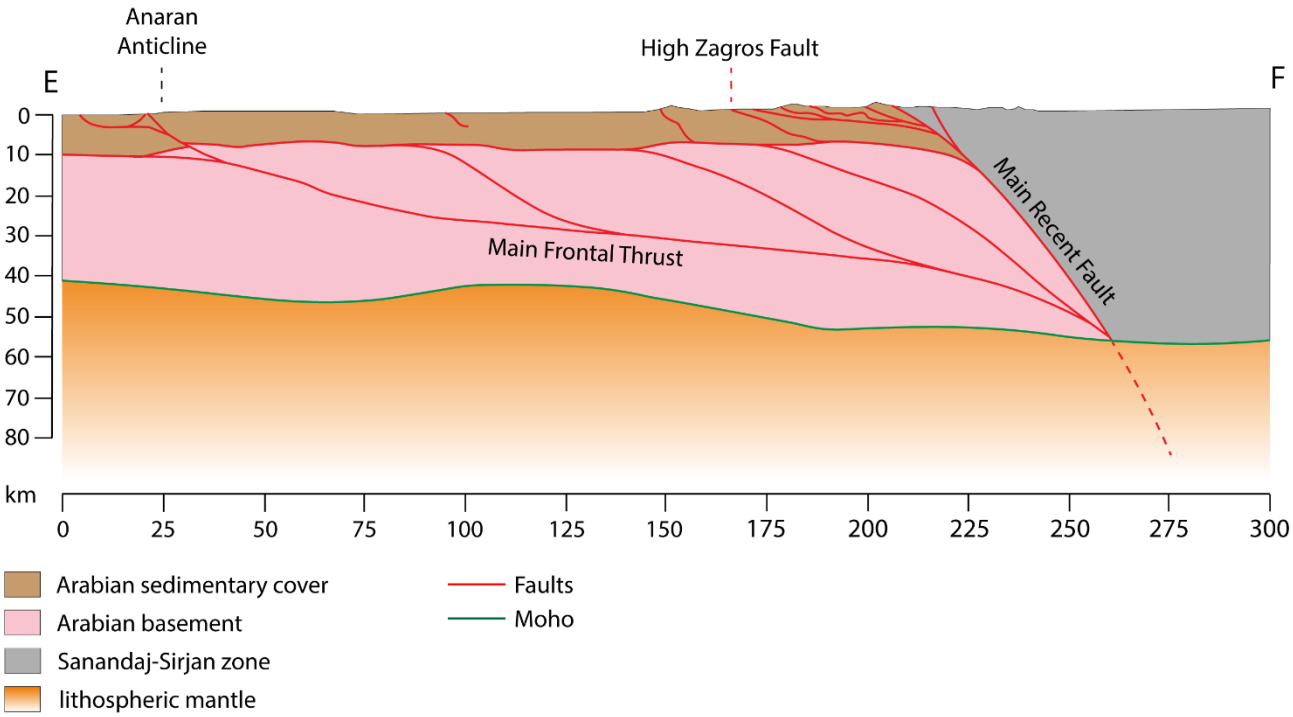

Figure 9 – Published geological cross section by Vergés et al. (2011a), EF segment in Figure 6. The entire sedimentary cover was unified in a unique unit (Basilici et al., 2019; 2020a; 2020b). Moho depth and geometry are constrained by Paul et al. (2010).

3.2 – Methods and Results

In Figure 10 is shown the 2-D geological model (GH segment in Figure 6). It was implemented on the basis of the geological section by Tavani et al. (2018a; Figure 7) because its location crosses the epicentre of 12 November 2017 earthquake (Mw = 7.3). In order to include the entire MFT in the section, this was integrated with the two further section by Tavani et al. (2020; Figure 8) and Vergés et al. (2011a; Figure 9). Moho depth and geometry are included in the 2-D model by using a projection of the Moho calculated by Paul et al. (2010).

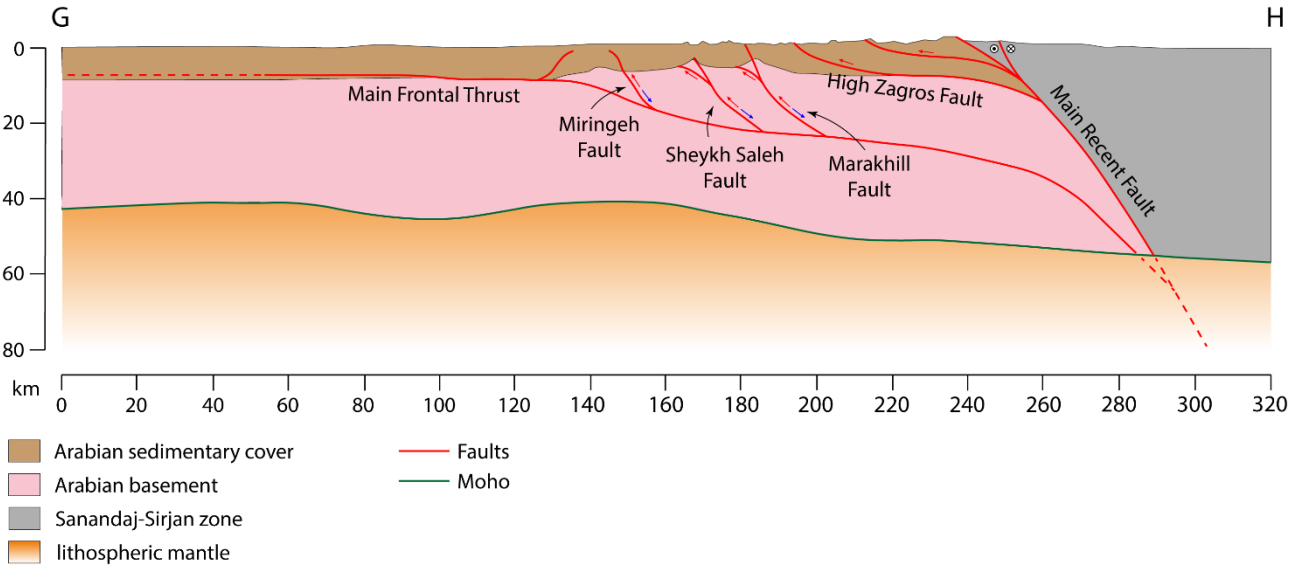

Figure 10 – 2-D Model (GH segment in Figure 6). This composite section was built by integrating sections by Tavani et al. (2018a; Figure 7) for the northern sector, by Tavani et al. (2020; Figure 8) for the central section and by Vergés et al. (2011a; Figure 9) for the southern sector. The Moho was projected using profile by Paul et al. (2010). The crust of the model was subdivided into three different homogeneous zone as shown in the legend (modified by Basilici et al., 2019; 2020a; 2020b).

Putting the 2-D model (Figure 10) and the published balanced geological cross section (Figures 7, 8 and 9) in prospective into a 3-D space (Figure 11), it was possible to build a 3-D geological model of the Lurestan arc (blue rectangle in Figure 6). The used 3-D space covered an area of 320 km × 240 km, approximately as the area of the entire Lurestan arc. The chosen model's depth was 80 km in order to provide a better view of the entire crust and part of the lithospheric mantle. The 3-D model was built using Blender, a free and opensource 3-D computer graphics software downloadable

in its official website (https://www.blender.org; last access: 26 December 2020). Blender's features include 3-D modelling, fluid simulation and particle simulation and it was recently used to show complex 3-D geometries in many fields of study including geology (Basilici et al., 2020a; Florinsky and Filippov, 2019).

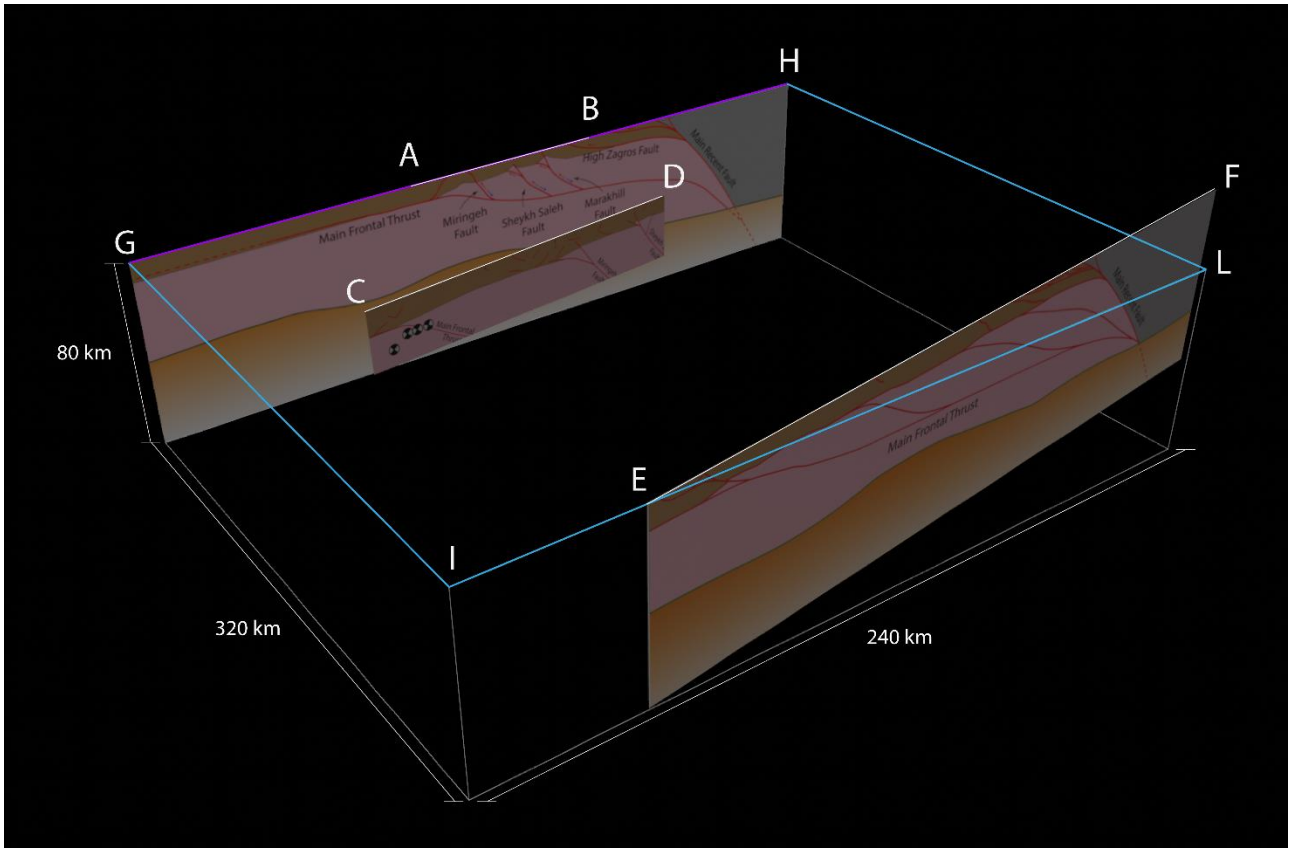

Figure 11 – Prospective of 2-D model (Figure 10) and published balanced geological cross section by Tavani et al. (2018a; Figure 7), Tavani et al. (2020; Figure 8) and Vergés et al. (2011a; Figure 9) into a 3-D space. The Violet line and the blue rectangle represent the 2-D model and the 3-D model area respectively (Figure 6).

The 3-D model (Figure 12) results in a volume of 6,144,000 (320 × 240 × 80) km^3 of rock. The topography was integrated using a 30 m resolution ASTER GDEM. The model took into account the MRF and MFT, while minor faults were not included to simplify the modelling procedure. In this 3-D case the crustal thickness was included using the 3-D Moho depth and geometry calculated by Jiménez-Munt et al. (2012).

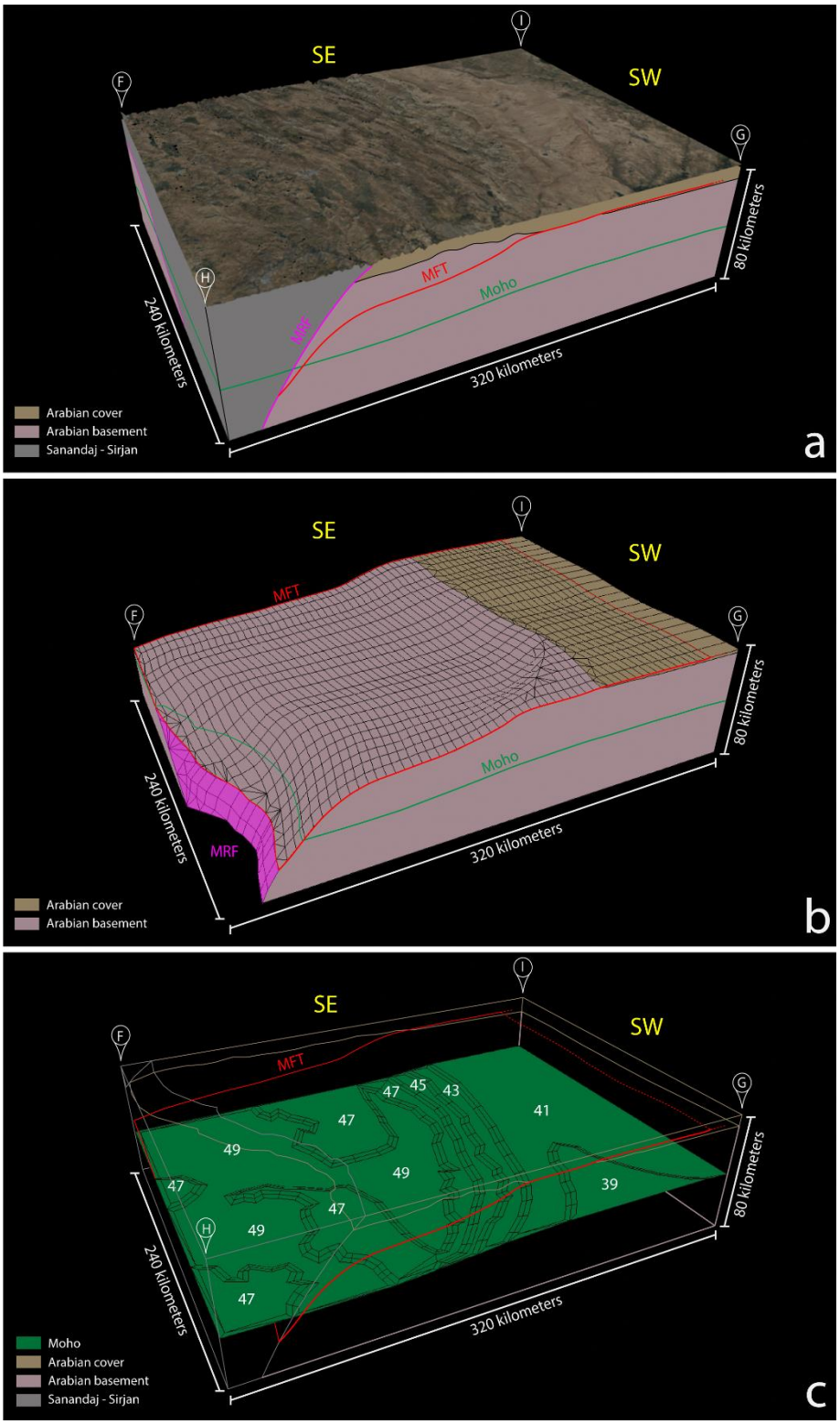

Figure 12 – 3-D geological model (modified from Basilici et al., 2020a) (a) Complete 3-D model of 6,144,000 (320 × 240 × 80) km^3 of rock volume, based on geological section by Tavani et al. (2018a; Figure 7), Tavani et al. (2020; Figure 8) and Vergés et al. (2011a; Figure 9). Topography is from a 30 m resolution ASTER GDEM. (b) MFT footwall topography (red line) including deep sector beneath the branch line with the MRF (violet line). (c) Moho geometry based on Jiménez-Munt et al. (2012), with Moho depth in km (white numbers). In order to provide a better view of MRF and MFT geometry, the lithospheric mantle is not shown as a different block beneath the Moho discontinuity.

4 – 2-D and 3-D Geothermal Models

To obtain a better knowledge of the Zagros thrust belt and the impact of the MFT on the thermal structure of the Lurestan arc, we improved an analytical methodology which took into account the temperature variation due to the re-equilibrated conductive state after thrusting. Frictional heating, heat flow density data, and a series of geologically derived constraints are used in the model. The mathematical procedure is based on available information about Moho (Francois et al., 2014; Jiménez-Munt et al., 2012; Paul et al., 2010) and thermophysical characteristics of rocks (Byerlee, 1967, 1978; Tunini et al., 2015). The analytical methodology was applied on the 2-D geological model presented in the previous chapter to obtain geotherms and isotherms (Basilici et al., 2019). The resulting 2-D geothermal model was compared with the numerical results obtained by previous studies (Kargaran and Neubauer, 2015; Shekarifard et al., 2012; Tunini et al., 2015). Subsequently, the same procedure was applied on the 3-D geological model presented on the previous chapter to elaborate the first 3-D model reproducing the thermal structure of the Lurestan arc (Basilici et al., 2020a).

4.1 – Previous Studies on Thermal Structure

Several authors studied the thermal structure of the Zagros complex and adjacent zones, resulting in a series of models in which they calculated surface heat flow, isotherms, geotherms and thermomechanical scenarios for the Zagros collision zone (Főrster et al., 2010; Francois et al., 2014; Kargaran and Neubauer, 2015; Schutz et al., 2014; Shekarifard et al., 2012; Tunini et al., 2015; Vernant and Chéry, 2006). Vernant and Chèry (2006) adopted a surface heat flow of Q_S = 40 mW/m^2, assuming radiogenic sources in the crust, and a mantle heat flow of Q_m = 10 mW/m^2 to calculate the first thermal field of the Zagros thrust belt used to produce a 2-D mechanical finite element

model. Főrster et al. (2010) calculated geotherms of the Arabian Shield in Jordan based on density, thermal conductivity and radiogenic heat production of a unique set of samples from uppermost crust down to the lithospheric mantle. Shekarifard et al. (2012) produced a 1-D thermal model of Alborz (Northern Iran) based on physical/chemical equations and geological assumptions to reconstruct burial and thermal history, taking into account different tectonic scenarios. Schűtz et al. (2014) calculated heat flow in Mesozoic sediments of Central and Southern Israel using the classical approach of heat-flow determination by implementing in the analysis high-precision continuous temperature logs obtained in air- and/or water filled boreholes. Francois et al. (2014) produced a series of 2-D numerical models of the Zagros/Central Iran to investigate the continental subduction and to explain the current topographic uplift, incorporating a free upper surface erosion, rheological stratification, brittle-elastic-ductile rheologies, metamorphic phase changes and account for the specific crustal and thermal structure of the Arabian and Iranian continental lithospheres. Kargaran and Neubauer (2015) investigated the lithospheric thinning and subsequent formation of the Iranian plateau using a 2-D numerical modelling, taking into account heat flow and mineral thermobarometry behaviour from west to east. Tunini et al. (2015) applied a combined geophysical-petrological methodology in order to study the thermal, compositional, density and seismological structure of the crust and upper mantle along two transect across the Arabia-Eurasia collision region. They calculated a 2-D numerical model of thermal structure showing isotherms from surface to asthenosphere.

4.2 – Constraints and Assumptions

Molnar et al. (1983) considered three sources of heat that affect the temperature in a region of thrust faulting: heat supplied from the mantle, radiogenic heating within the crust and frictional heating along the fault. The effect of these three source of heating can be isolated from one another, treated separately, and then combined.

The analytical procedure was applied on a series of pseudo-well (Figure 13) traced on geological models both 2-D and 3-D. Subsequently, we interpolated the model data by a second-order power-law polynomial equation, obtaining the best-fit analytical curves approximating the geothermal values. In the case of the 3-D model, we constructed isothermal surfaces using the minimum curvature spline interpolation technique (Basilici et al., 2019, 2020a).

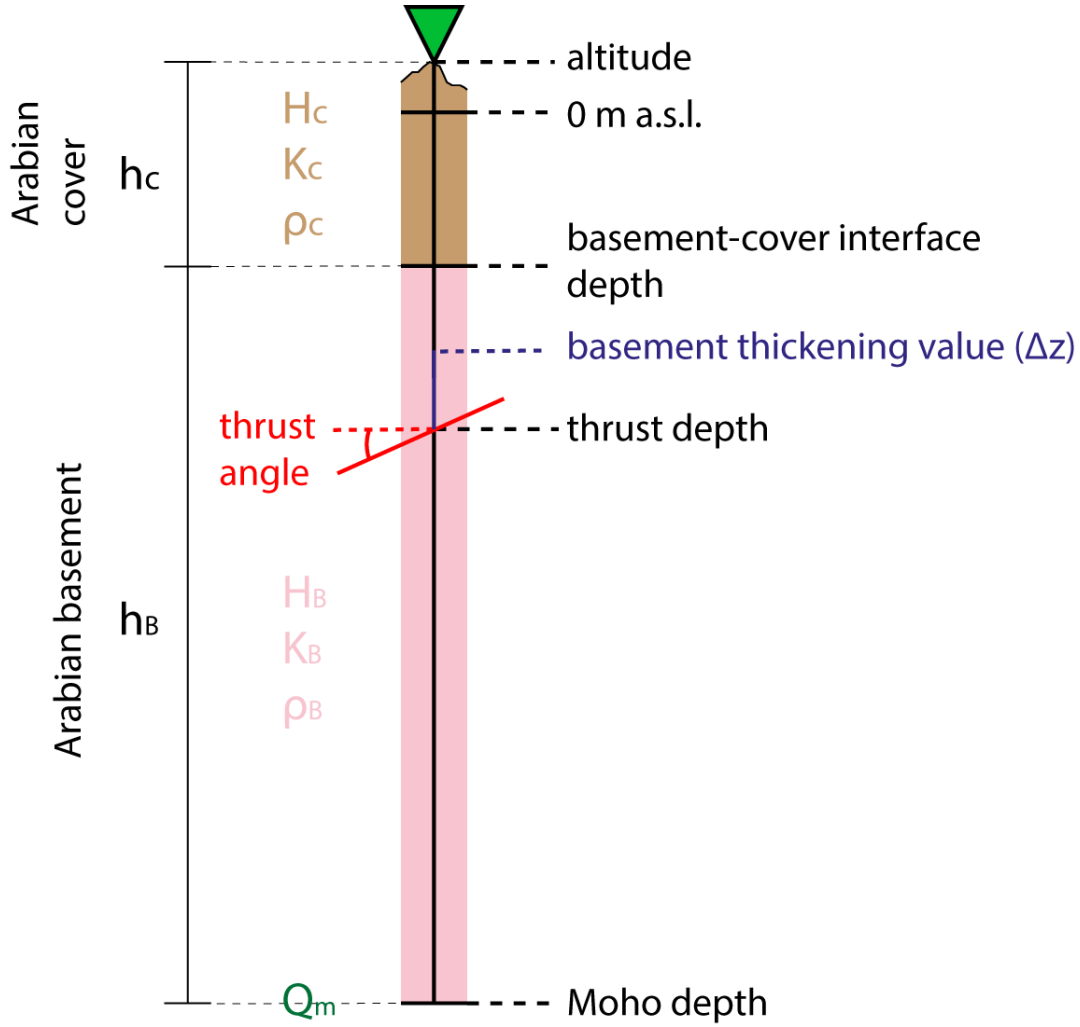

Figure 13 – Pseudo-well representation (modified from Basilici et al., 2019). Q_m is the heat flux at Moho; ρ_b and ρ_b are density of the sedimentary cover and basement, respectively; K_C and K_B are thermal conductivity for the sedimentary cover and basement, respectively; H_C and H_B are heat production rates for sedimentary cover and basement, respectively; Δ_Z is the basement thickening value.

To perform the 2-D geothermal model we considered five pseudo-wells in total (2, 3 and 4 are shown in Figure 14) located along the 2-D geological model presented

in the previous chapter (Figure 10, GH segment in Figure 6). For each pseudo-well we considered the following parameters and assumption:

1. Altitude. The surface was considered as flat at 0 m.a.s.l.
2. Thickness of the Arabian cover (h_C). We considered a constant thickness of the sedimentary cover of 7.5 km. The density of the Arabian cover was fixed to ρ_C = 2.55 × 10^3 kg/m^3 (Teknik et al., 2019).
3. Thickness of the Arabian basement (h_B). We considered a variable thickness of the basement based on the depth of the Moho discontinuity calculated by Paul et al. (2010). The density of the basement was fixed to ρ_b = 2.80 × 10^3 kg/m^3 (Teknik et al., 2019).
4. Thrust depth and angle. The pseudo-wells cross the MFT at different depths with a certain angle.
5. Amount of basement offset by the MTF (Δ_Z). Taking into account the reconstructed geometry of the Arabian margin by Le Garzic et al. (2019), the timing of activity of the faults in our 2-D geological model (Figure 10) is variable and it is divided into three steps: (i) Campanian/Maastrichtian, 84 – 66 Ma for the MZT and HZF, (ii) Miocene, 20 – 10 Ma for the MRF and the Marakhil, Seykh Saleh, and Miringeh faults, and (iii) 10 Ma-Present for the MFT. We considered a total shortening of 20 km in the range of 20 – 10 Ma. The resulting slip rate (v) and the basement thickening were in the range of 1 – 2 mm yr^{-1} and 3.5 – 5.8 km respectively (Basilici et al., 2019; 2020a). The friction coefficient (μ) was fixed to 0.6 according to Byerlee (1967; 1978).
6. Constant heat production rate for the sedimentary cover (H_C) = 1.0 µW/m^3 (Tunini et al., 2015).
7. Constant heat production rate for the basement (H_B) = 0.4 µW/m^3 (Tunini et al., 2015).
8. Thermal conductivity for the sedimentary cover (K_C) = 2.0 $Wm^{-1}K^{-1}$ (Tunini et al., 2015).

9. Thermal conductivity for the basement (K_B) = 2.2 $Wm^{-1}K^{-1}$ (Tunini et al., 2015).
10. Heat flux at the Moho (Q_m) = 20 mW/m^2 (Francois et al., 2014). However, taking into account that higher values have been proposed for the Red Sea zone of the Arabian plate (Főrster et al., 2010; Schütz et al., 2014), a value of (Q_m) = 25 mW/m^2 was also considered in the calculation of the geotherms along our profile.

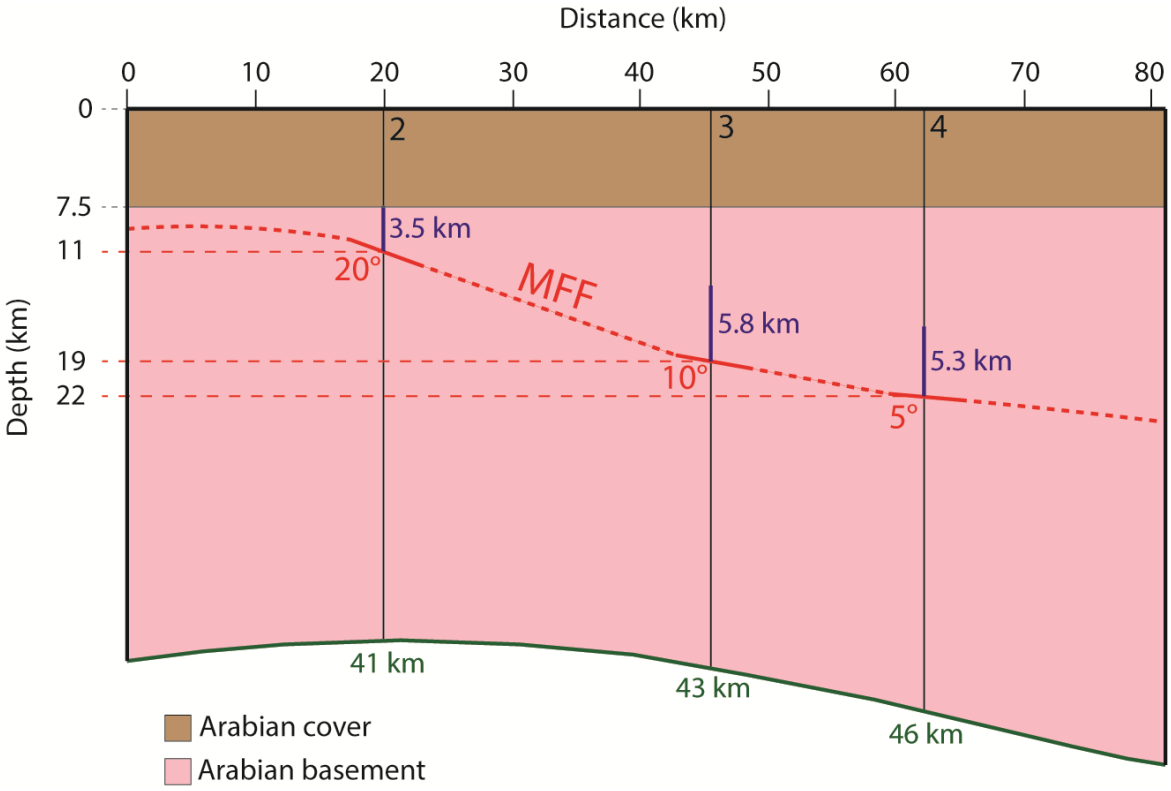

Figure 14 – Conceptual model for geothermal calculation along the 2-D geological model (Figure 10, GH segment in Figure 6, modified from Basilici et al., 2019). The graph describes the parameters used in the analytical calculation: Crustal thickening values (Δ_Z) are identified by blue numbers, thrust angles by red numbers and Moho depth values by green numbers.

To perform the 3-D geothermal model we considered a series of twenty pseudo-wells (Figure 15) located into the 3-D geological model presented in the previous chapter (the blue rectangle in Figure 6). For each pseudo-well it was considered the same parameters and assumptions used to perform the 2-D geothermal model but here it was improved the analytical procedure including altitude (taking into account the topography by a 30 m resolution ASTER GDEM) and the depth of the Moho discontinuity calculated by Jiménez-Munt et al. (2012) in which the 3-D geometries of

the crust-mantle interface is visible. The thickness of the Arabian cover was considered as variable based on the 3-D geological model (Figure 12).

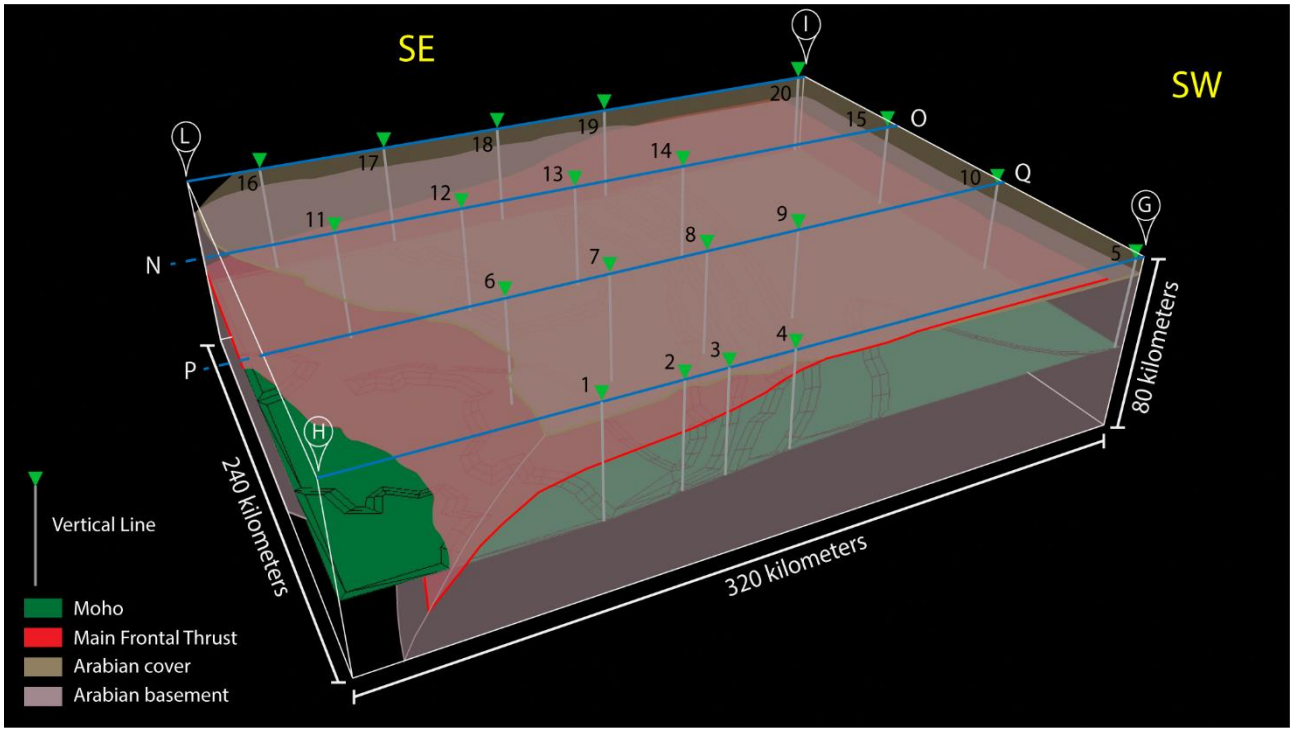

Figure 15 – The 3-D geological model (Figure 12, blue rectangle in Figure 6, modified from Basilici et al., 2020a) with the location of pseudo-wells. The grey pseudo-wells are numbered from 1 to 20. The section traces (blue lines, HG, PQ, NO, LI) were used to perform the analytical procedure.

4.3 – Analytical Procedure

In the ideal case with no thrusts, we obtain the following equations of heat flow

$$\mathrm{Q(z)} = Q_m + H_B h_B + H_C(h_C - z),\ 0 \leq z \leq h_c \quad (1)$$

$$\mathrm{Q(z)} = Q_m + H_B(h_C + h_B - z),\ h_C \leq z \leq h_c + h_B \quad (2)$$

In the hypothesis of a constant heat production rate for the cover (H_C) and the basement (H_B), the equations of temperature for the two layers are:

$$\mathrm{T(z)} = \left(\frac{Q_m + H_B h_B + H_C h_C}{K_C}\right) z - \frac{H_C}{2K_C} z^2,\ 0 \le z \le h_c \quad (3)$$

$$\mathrm{T(z)} = \mathrm{T}(h_C) + \left(\frac{Q_m + H_B h_B}{K_C}\right)(z - h_C) - \frac{H_B}{2K_C}(z - h_C)^2,\ h_C \le z \le h_c + h_B \quad (4)$$

where:

$$\mathrm{T}(h_C) = \left(\frac{Q_m + H_B h_B}{K_C}\right) h_C + \frac{H_C}{2K_C} {h_C}^2 \quad (5)$$

Assuming a single slip basement thrusting, besides generating a new source of heat due to friction along the fault, produces a perturbation in the propagation of the mantle heat and an increase in radiogenic heat within the basement (Basilici et al., 2019; 2020a; Candela et al., 2015). In the calculation of the heat source represented by frictional heating associated with thrust faulting, the shear stress (ϑ) was considered, which was obtained by Sibson's (1974) formulation for favourable oriented thrust faults at the chosen depths under hydrostatic pore-fluid conditions with a fixed friction coefficient.

The heat flow and the temperatures for the two units of the model are obtained by the following equations:

$$\mathrm{Q(z)} = Q_m + H_B {h'}_B + H_C(h_C - z) + \vartheta v\ ,\ 0 \le z \le h_c \quad (6)$$

$$\mathrm{Q(z)} = Q_m + H_B({h'}_B + h_C - z) + \vartheta v\ ,\ h_C \le z \le z_0 \quad (7)$$

$$\mathrm{Q(z)} = Q_m + H_B({h'}_B + h_C - z)\ ,\qquad z_0 < z \le h_C + {h'}_B \quad (8)$$

where ${h'}_B = h_B + \Delta z$, v is the average slip rate along the thrust, and ϑ is the shear stress at the thrust depth z_0.

In the case of thrusting, the procedure to compute the temperature follows the analytical method developed by Molnar et al. (1983):

$$T(z,t) = T(z,\infty) - \theta(z,t) \quad (9)$$

where $T(z,t)$ is the new equilibrium state, $T(z,\infty)$ is the final temperature of the new equilibrium status ($t \to \infty$), and $\theta(z,t)$ is the time dependent term. Furthermore, $\theta(z,t)$ is calculated by the followed equations:

$$\theta(z,t) = \sum_{n=0}^{\infty} A_n \, sin(a_n z) e^{-a_n^2 K t} \quad (10)$$

where

$$A_n = \frac{2}{h} \int_0^h \theta(z,0) \, sin(a_n z) \, dz \quad (11)$$

with

$$a_n = \frac{(2n+1)}{2h} \quad (12)$$

and $\theta(z,0)$ is the perturbed initial state, which depend on the heat source type, the thrust depth (z_0), the crustal thickness (h), the thermal capacity (k), and diffusivity (K). Therefore, the parameter of the perturbed initial $\theta(z,0)$ is used to compute the coefficient A_n (Equations (3)), then time dependent term $\theta(z,t)$ (Equations (2)), and lastly the time dependent temperature adding the final temperature (Equations (1)). In particular, the terms $T(z,\infty)$ and $\theta(z,t)$ of the equation (1) depend on the thermal source type and on thrusting involving the sedimentary cover (Basilici et al., 2019; 2020a; Megna et al., 2014) or the basement (Basilici et al., 2019; 2020a; Candela et al., 2015).

To compute the geotherms the calculation is separated into two parts, one for the sedimentary cover ($z \leq h_C$) and another for the basement ($h_C < z \leq h_C + h'_B$). In the

basement the new perturbed conductive status associated with two principal heat sources – i.e. mantle heat flow (MH) and basement radiogenic heat (RH_B) – and the additional heat source due to friction on the fault (FH) are considered. For the sedimentary cover, the basement radiogenic heat increment at the bottom of this layer, as a consequence of basement overthrusting in addition to the previous equilibrium status (DH) and the crustal radiogenic heat (RH_C), is estimated. Moreover, for this layer the temperature increases due to friction source (FH). This approach can be mathematically summarized as follows:

$$\mathrm{T(z,t)} = T_{DH}(z,t) + T_{RH_C}(z) + T_{MH}(z,t) + T_{FH}(z,t), \quad 0 \leq z \leq h_c \tag{13}$$

$$\mathrm{T(z,t)} = T_{DH}(t) + T_{RH_C} + T_{RH_B}(z,t) + T_{MH}(z,t) + T_{FH}(z,t), h_C < z \leq h_c + h'_B \tag{14}$$

where $T_{DH}(t)$ and T_{RH_C} are the respective temperatures calculated at the top of the basement ($z = h_C$). In particular, $T_{RH_C}(z)$, the only not-time-dependent term, is the temperature due to the radiogenic heat in the cover layer. Considering the overthrusting, $T_{RH_B}(z,t)$ is the temperature associated with the perturbed radiogenic heat in the basement, whereas $T_{MH}(z,t)$ and $T_{FH}(z,t)$ are the temperatures associated with the new perturbed state of the mantle and of the new heat source due to overthrusting. Therefore, based on analytical method developed by Molnar et al. (1983), each time-dependent term has the following generic expression:

$$T_{XH}(z,t) = T_f(z) - \sum_0^\infty A_n \sin(a_n z) e^{-a_n^2 Kt} \tag{15}$$

with

$$\mathrm{X} \equiv \mathrm{D, R, M, F} \tag{16}$$

In this study, instead, Molnar et al. (1983) equations are modified considering a constant radiogenic heat for the two layers (Tunini et al., 2015; Basilici et al., 2019; 2020a; table 1).

Without the contribution of the frictional heat, the final temperature for the sedimentary cover is given by:

$$T_{DH}(z,\infty) + T_{RH_C}(z) + T_{MH}(z,\infty) = \left(\frac{Q_m + H_B h'_B + H_C h_C}{K_C}\right) z - \frac{H_C}{2K_C} z^2,\ 0 \le z \le h_c \quad (17)$$

and the perturbed initial state associated uniquely with the radiogenic heat increase is given by

$$\theta_{DH}(z,0) = \left(\frac{H_B \Delta_z}{K_C}\right) z \quad (18)$$

whereas the perturbed initial state associated with the mantel heat is given by

$$\theta_{MH}(z,0) = \left(\frac{Q_m \Delta_z}{K_C}\right) z \quad (19)$$

Considering only the contribute of the basement radiogenic source, the final temperature for the basement is given by:

$$T_{RH_B}(z,\infty) = \left(\frac{H_B h'_B}{K_B}\right)(z - h_C) - \frac{H_B}{2K_B}(z - h_C)^2, \quad h_C < z \le h'_B \quad (20)$$

and the perturbed initial state associated uniquely with increased basement thickness is given by:

$$\theta(z,0) = \left(\frac{H_B \Delta_z}{K_B}\right)(z - h_C), \qquad h_C < z \le z_0 \quad (21)$$

$$\theta(z,0) = \left(\frac{H_B h'_B}{K_B}\right)(z_0 - h_C) - \frac{H_B}{2K_B}(z_0 - h_C)^2 - \left(\frac{H_B(h'_B - \Delta_z)}{K_B}\right)(z_0 - h_C - \Delta_z) + \frac{H_B}{2K_B}(z_0 - h_C - \Delta_z)^2, \qquad z_0 \le z \le h'_B \tag{22}$$

For both units of the model, the perturbation of the mantle-derived heat flow causes small temperature changes (Basilici et al., 2019; Candela et al., 2015). The temperature increment due to frictional heating is added as follows:

$$T_{FH}(z,\infty) = \theta(z,0) = \frac{\vartheta v}{K_C} z, \quad 0 \le z < h_C \tag{23}$$

$$T_{FH}(z,\infty) = \theta(z,0) = \frac{\vartheta v}{K_B} z, \quad h_C \le z < z_0 \tag{24}$$

$$T_{FH}(z,\infty) = \theta(z,0) = \frac{\vartheta v}{K_B} z_0, \quad z_0 \le z \le h_C + h'_B \tag{25}$$

and in this latter case the final temperature coincides with the perturbed initial state.

The table 1 is the list of the terms T_f, a_n, and A_n for each source type, dividing the compute of the temperatures for the cover layer ($0 \le z \le h_C$), and for hanginwall ($h_C < z \le z_0$) and footwall ($z_0 < z \le h_C + h'_B$) of the thrust in the basement.

		$0 \le z \le h_C$	$h_C < z \le z_0$	$z_0 < z \le h_C + h'_B$
$T(z,t)$		$T_{DH}(z,t) + T_{RH_C}(z) + T_{MH}(z,t) + T_{FH}(z,t)$	$T_{DH}(t) + T_{RH_C} + T_{RH_B}(z,t) + T_{MH}(z,t) + T_{FH}(z,t)$	$T_{DH}(t) + T_{RH_C} + T_{RH_B}(z,t) + T_{MH}(z,t) + T_{FH}(z,t)$
T_{DH}	T_f	$\frac{H_B h'_B}{K_C} z$	$\frac{H_B h'_B}{K_C} h_C$	$\frac{H_B h'_B}{K_C} h_C$
	a_n	$\frac{(2n+1)\pi}{2h_C}$	$\frac{(2n+1)\pi}{2h_C}$	$\frac{(2n+1)\pi}{2h_C}$
	A_n	$\frac{2H_B \Delta z}{K_C h_C a_n^2} \sin(a_n h_C)$	$\frac{2H_B \Delta z}{K_C h_C a_n^2} \sin(a_n h_C)$	$\frac{2H_B \Delta z}{K_C h_C a_n^2} \sin(a_n h_C)$
T_{RH_C}		$\frac{H_C h_C}{K_C} z - \frac{H_C}{2K_C} z^2$	$\frac{H_C}{2K_C} {h_C}^2$	$\frac{H_C}{2K_C} {h_C}^2$
T_{RH_B}	T_f		$\frac{H_B h'_B}{K_B} z - \frac{H_B}{2K_B} z^2$	$\frac{H_B h'_B}{K_B} z - \frac{H_B}{2K_B} z^2$
	a_n		$\frac{(2n+1)\pi}{2h'_B}$	$\frac{(2n+1)\pi}{2h'_B}$
	A_n		$\frac{2H_B \Delta z}{K_B h'_B a_n^2} \left[\sin(a_n z_0) + a_n \left(h'_B - z_0 - \frac{\Delta z}{2}\right) \cos(a_n z_0)\right]$	$\frac{2H_B \Delta z}{K_B h'_B a_n^2} \left[\sin(a_n z_0) + a_n \left(h'_B - z_0 - \frac{\Delta z}{2}\right) \cos(a_n z_0)\right]$
T_{MH}	T_f	$\frac{Q_m}{K_C} z$	$\frac{Q_m}{K_B} z$	$\frac{Q_m}{K_B} z$
	a_n	$\frac{(2n+1)\pi}{2(h_C + h'_B)}$	$\frac{(2n+1)\pi}{2(h_C + h'_B)}$	$\frac{(2n+1)\pi}{2(h_C + h'_B)}$
	A_n	$\frac{2Q_m \Delta z}{K_C (h_C + h'_B) a_n} \cos(a_n z_0)$	$\frac{2Q_m \Delta z}{K_B (h_C + h'_B) a_n} \cos(a_n z_0)$	$\frac{2Q_m \Delta z}{K_B (h_C + h'_B) a_n} \cos(a_n z_0)$
T_{FH}	T_f	$\frac{\sigma v}{K_C} z$	$\frac{\sigma v}{K_B} z$	$\frac{\sigma v}{K_B} z_0$
	a_n	$\frac{(2n+1)\pi}{2(h_C + h'_B)}$	$\frac{(2n+1)\pi}{2(h_C + h'_B)}$	$\frac{(2n+1)\pi}{2(h_C + h'_B)}$
	A_n	$\frac{2\sigma v}{K_C (h_C + h'_B) a_n^2} \sin(a_n z_0)$	$\frac{2\sigma v}{K_B (h_C + h'_B) a_n^2} \sin(a_n z_0)$	$\frac{2\sigma v}{K_B (h_C + h'_B) a_n^2} \sin(a_n z_0)$

Table 1 – Terms of the equations used for the analytical procedure (Basilici et al., 2020a).

4.4 – Geothermal Model Results

We calculated surface heat flow $Q_s(Q_s = \mathrm{Q}(0))$, isotherms and geotherms along the 2-D geological model (Figure 10). In Figure 16a we show the surface heat flow Q_s for a (Q_m) = 20 mW/m^2 obtained using an interpolation of a second-order power-law polynomial equation which takes into account the value calculated using five pseudo-wells. The heat flow increases its value from the point G to the point H due to the heat flow produced by MFT friction (T_{FH}), basement thickening (h'_B) and deepening of the Moho. The resulting surface heat flow ranges from ~41 to ~ 65 mW/m^2 (Basilici et al., 2019). Into the undeformed Arabian plate the temperature increases constantly, moving to point H the temperature shows an increment due to thrusting and deepening of the Moho. The temperature increase from ~400°C at 30 km depth along pseudo-well 1, to ~500°C at the same depth along pseudo-well 5, where the MFT offset occurred at greater depths (Basilici et al., 2019).

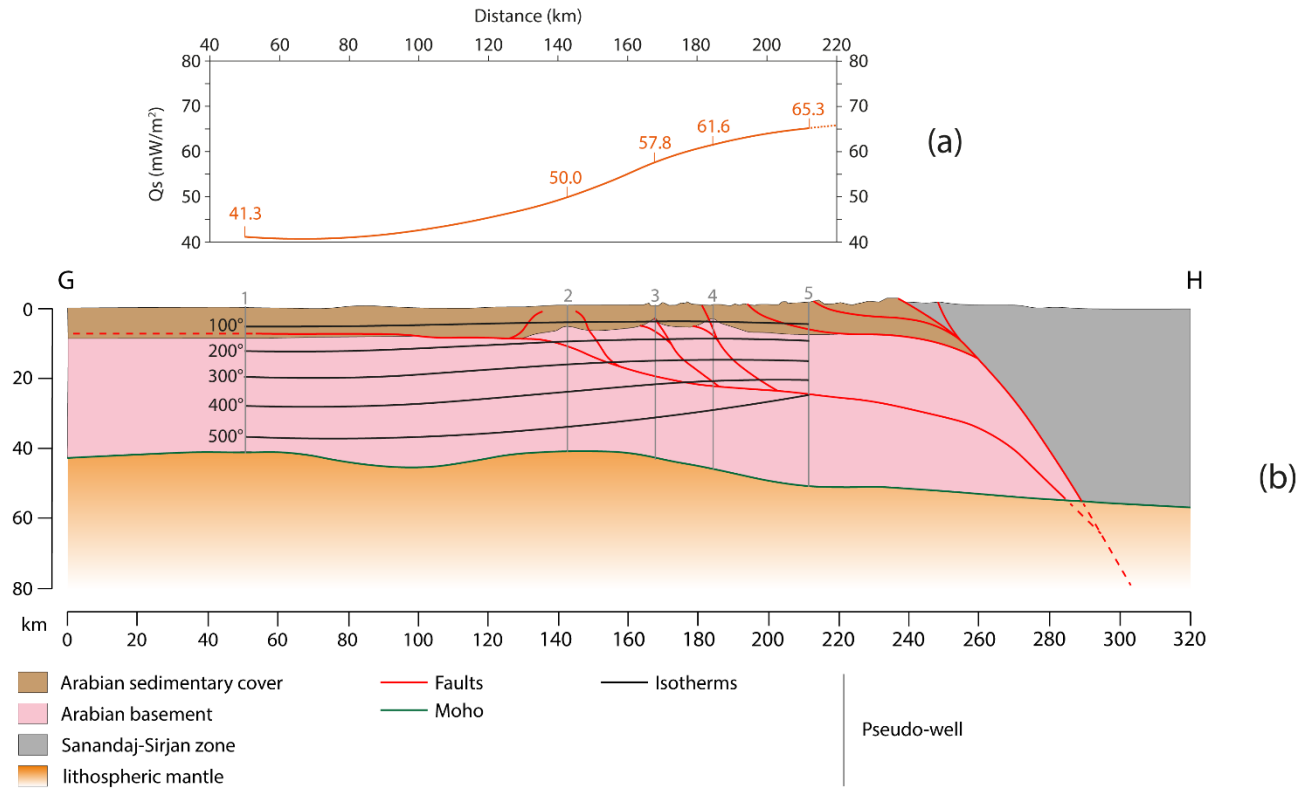

Figure 16 – (a) Surface heat flow (Q_s) for a (Q_m) = 20 mW/m^2 calculated using five pseudo-wells. (b) 2-D thermal structure of the Zagros thrust belt for a (Q_m) = 20 mW/m^2 (modified from Basilici et al., 2019).

In Figure 17 we show geotherms for (Q_m) = 20 mW/m^2 and (Q_m) = 25 mW/m^2. With the same Q_m, the absence of thrust is visible in the geotherm relative to pseudo-well 1 that shows a constant increment of temperature with depth. The geotherm relative to pseudo-well 2 shows a smooth change with respect to that pseudo-well 1 because of the basement thickening as a result of thrusting. On the other hand, geotherms relative to pseudo-wells 3, 4 and 5 have higher gradients due to the presence of thrust at greater depths. Moreover, variations between geotherms for (Q_m) = 20 mW/m^2 and (Q_m) = 25 were computed for pseudo-wells 2,3 and 4, in order to examinate temperature changes. These variations increase with depth, resulting in a maximum values of ~100 °C at depth of ~45 km (Figure 17; Basilici et al., 2019).

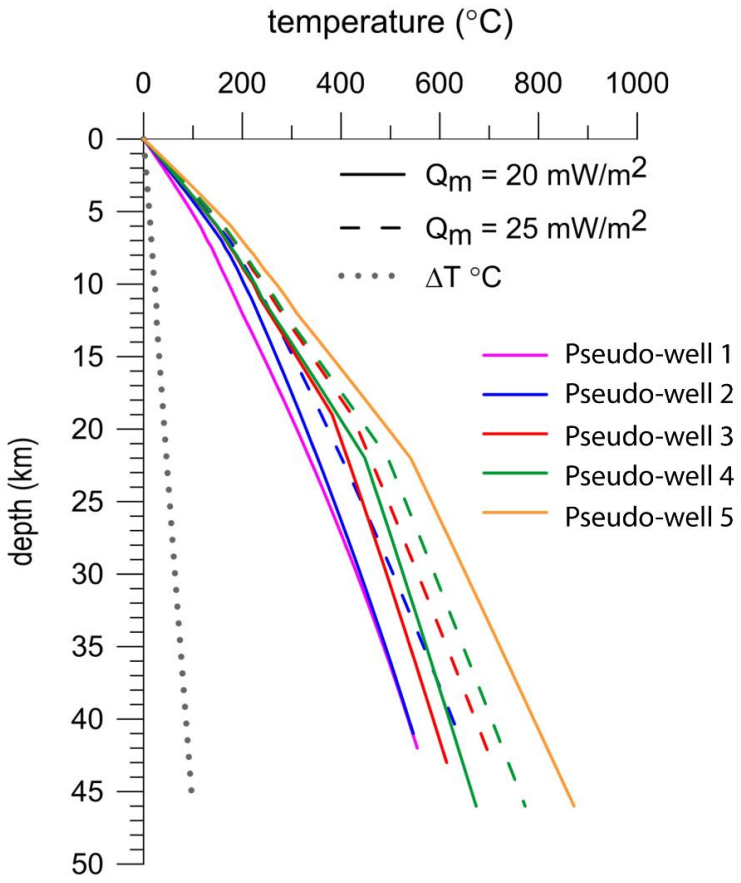

Figure 17 – Calculated geotherms corresponding to the five pseudo-wells shown in Figure 16 for a (Q_m) = 20 mW/m^2 (solid lines) and (Q_m) = 25 mW/m^2 (dashed lines, for the pseudo-well 1 it was not calculated). The maximum change of temperature $\Delta T_{(z)}$ between the two geotherms with (Q_m) = 20 mW/m^2 and (Q_m) = 25 mW/m^2 is indicated by the dotted grey line (modified from Basilici et al., 2019).

Megna et al. (2014) pointed out that the largest temperature changes are obtained by varying the heat flow, while temperature changes are in the range of 2 – 5% when thickness, thrusting depth, thermal conductivity, timing of activity, and slip rate values vary by 10% of their initial chosen value (Basilici et al., 2019).

We calculated the geotherm for each pseudo-well of the 3-D geological model (Figure 12). The result is a series of twenty geotherms shown in Figure 18. For a better visualization of the results we produced four section (HG, PQ, NO, LI on Figure 19) on the 3-D geological model (Basilici et al., 2020a).

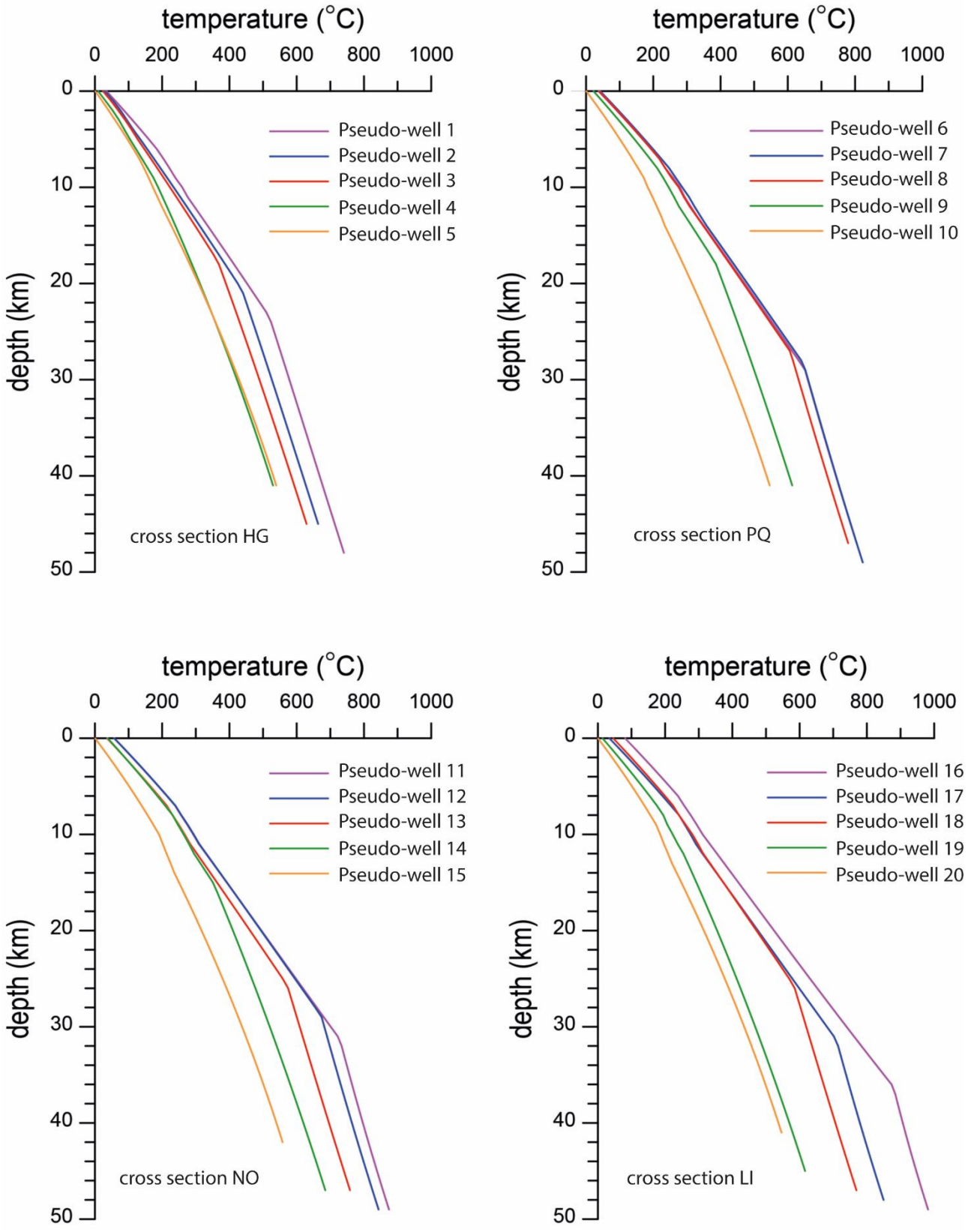

Figure 18 – Calculated geotherms corresponding for the twenty pseudo-wells shown on Figure 19. Each graph contains geotherms relative to the respective cross-sections HG, PQ, NO and LI (modified from Basilici et al., 2020a).

As observed on the 2-D model, the absence of thrust is visible by a constant increment of temperature with depth (geotherms relative to pseudo-wells 5, 10, 15 and 20 represented by yellow lines in Figure 18). A weaker temperature increase occurred for the geotherms of pseudo-wells 4, 9, 14 and 19 (green lines in Figure 18), where the thrust was shallower and implied a smaller amount (3.5 km) of basement offset. On the other hand, the other geotherms show an increase of temperature variation in correspondence to the MFT. In particular, the different trend of geotherms depended on both the basement thickness modified by thrusting (ΔT) and on the thrust depth (Basilici et al., 2020a). Megna et al. (2014) checked the sensitivity of this type of analytical procedure, a variation of about 10% of thrust depth or slip rate produces a change of frictional heat that modified the final temperature by values never exceeding 2%.

We interpolated the temperature data from 50°C to 500°C using a 50°C of step in order to provide a better overview of the temperature trend along each cross section (HG, PQ, NO and LI showed in Figure 19). The second-order power-law polynomial equation used to interpolate the data consisted of best-fit analytical curves with a rms (root mean square) error comprised between 0.6 and 3.75 (for the 100°C and 500°C isotherms, respectively; Basilici et al., 2020a).

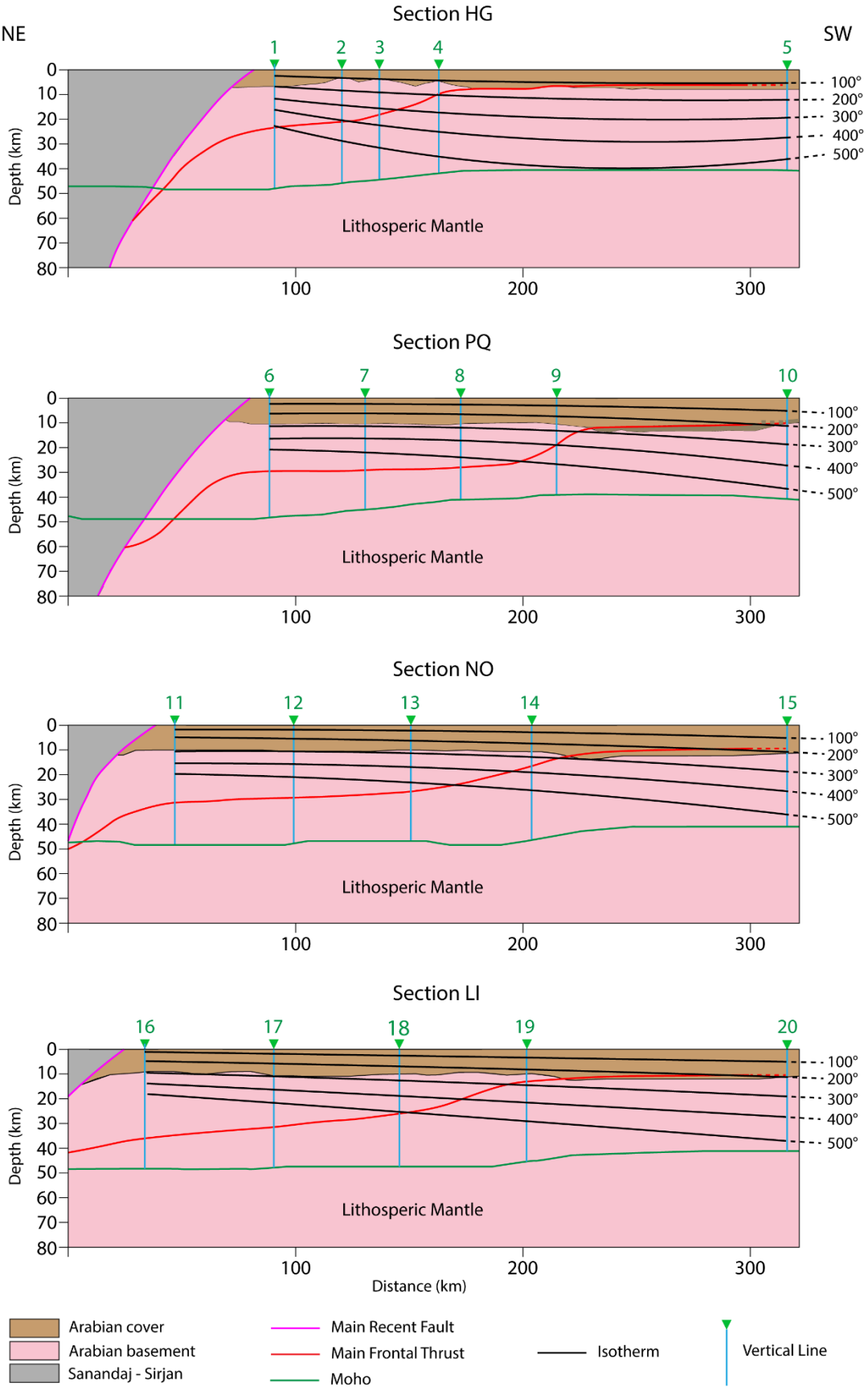

Figure 19 – Isotherms for the 100 – 500 °C temperature range (100°C steps) calculated using a second-order power-law polynomial interpolation for cross-sections HG, PQ, NO and LI (modified from Basilici et al., 2020a).

The isotherms shown in Figure 19 define a general trend of increasing temperature moving from SW to NE. Only the isotherm pattern along cross-section HG defined an upward curvature, the isotherm pattern along the other cross-sections show a gentle downward curvature, while more straight, SW-ward dipping isotherms characterize cross-section LI. The deepening of the isotherms involved depth changes in the range of ~ 20 km for the 100°C and 500°C respectively (Basilici et al., 2020b).

The thermal structure shows a clear correlation with the geometry of the MFT which is the main thrust fault of the region. According to Tavani et al. (2020), the MFT developed in the necking domain of the Jurassic rift system ahead of an array of inverted Jurassic extensional faults, the related structural architecture resembling that of a crustal-scale footwall shortcut. As the main crustal ramp of the MFT underlies at depth the MFF, the sinusoidal shape of the latter in the Lurestan region would derive from the re-use of the originally segmented, inverted Jurassic rift system (Tavani et al., 2020). Despite this long-lived paleo-tectonic control and the fundamental role underlying thrust (MFT) controlling it, are recent processes. These are dated to ca. 3 Ma based on stratigraphic information (Homke et al., 2004), and to ca. 5 Ma based on low-temperature thermochronology data (Koshnaw et al., 2017). According to the latter studies, the major morphotectonic feature constituting the Mountain Front Flexure developed during the Pliocene by basement-involved thrusting as deformation migrated downward at deeper crustal levels. Therefore, late-stage, crustal ramp-dominated thrusting (Butler and Mazzoli, 2006) not only led to the development of a prominent geomorphological boundary between the high Zagros Mountains and the low foothills to the SW (Berberian, 1995; Falcon, 1961; Emami et al., 2010) but also appears to have exerted a major control on the thermal structure of the Lurestan salient. Using the minimum curvature spline interpolation technique we constructed a series of isothermal surfaces, for the 100°C to 500°C isotherms (Figure 20). This technique shows a good fit with the second-order power-law polynomial interpolation (Basilici et al., 2020a). The Figure 20 shows how the first-order, general pattern of foreland-ward deepening of the isotherms was rendered more articulated by along-strike

variations, mainly consisting of a SE-ward climbing of the isotherms (Basilici et al., 2020a).

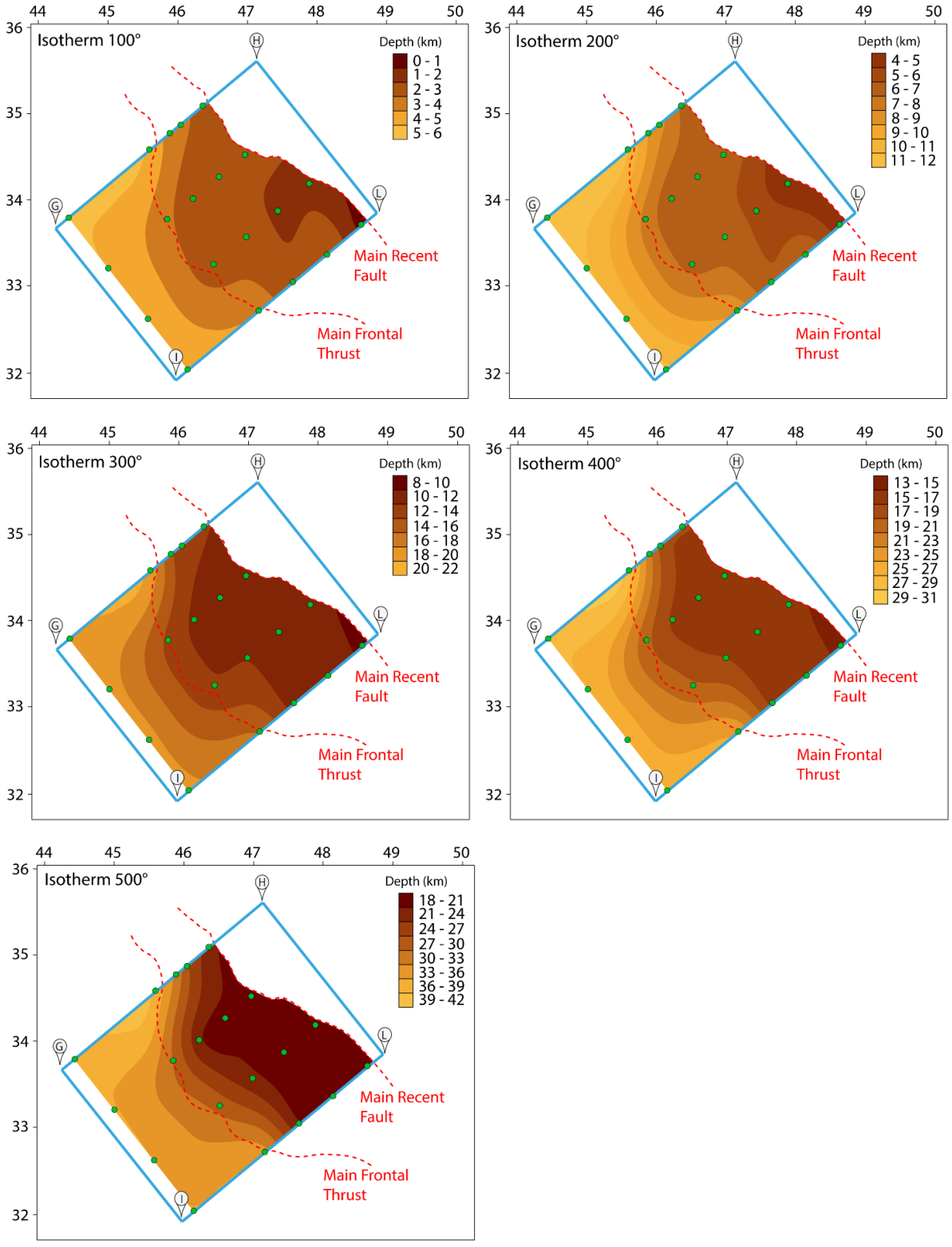

Figure 20 – Isotherm depth contour maps obtained by spline interpolation for the 100 – 500 °C temperature range (modified from Basilici et al., 2020a).

5 – 2-D Structural Finite Element Models

In order to unravel how and where co-seismic and inter-seismic deformation of the MFT impacts spatial and temporal patterns of rock uplift of a mountain range, a 2-D elastic finite element model along the 2-D geological model presented in chapter 3 (Figure 10) was performed (Basilici et al., 2020b). The aim of the finite element model (FEM) is to simulate inter-seismic stress and strain accumulation, and to obtain information about the vertical surface displacement associated with both inter-seismic and co-seismic stages in this region characterized by thrust-related seismicity.

5.1 – FEM Methodology and Previous Studies

The FEM methodology is actually one of the best methods to study complex systems in various study fields. In geophysics it has been successfully applied and validated by recent studies in different regions of the world (e.g. Candela et al., 2015; Carminati and Vadacca, 2010; Liu et al., 2015; Megna et al., 2005; 2008; Vigny et al., 2009; Zhu and Zhang, 2013). This method consists of the geometric construction of a model containing the fault setting of interest. To resolve the system, the model was divided into an equivalent assemblage of small finite elements (elementary components or mesh). As a result, for each element, a solution was formulated and combined to obtain the approximated solution for the entire system. The smaller the elementary components are, the closer the system is to the continuum case, the grater complexity of the solution becomes. Generally, it needs to research a good compromise between accuracy, numerical cost and complexity of the studied problem. At the end, a sensitivity analysis was carried out in order to quantify the solution error.

Several authors applied FEM methodology to understand the structural implications of the Zagros mountain (Austermann and Iaffaldano, 2013; Francois et

al., 2014; Tunini et al., 2015; Vernant and Chèry, 2006). Vernant and Chèry (2006) used a 2-D FEM to investigate the influence on the Zagros deformation of the obliquity of convergence, the rheological layering of the lithosphere and a possible weakness of the MRF. Calculating, as a result, the percentage of accommodation of the MRF. Austermann and Iaffaldano (2013) performed a global dynamic 2-D FEM of the mantle/lithosphere system to test the most recent uplift across the Arabia-Eurasia collision zone, including Zagros orogeny. Francois et al. (2014) produced a series of 2-D numerical models of the Zagros/Central Iran that incorporate free upper surface erosion, rheological stratification, brittle-elastic-ductile rheologies, and metamorphic phase change and account for the specific crustal structure of the Arabian and Iranian continental lithospheres. They tested the impact of the transition from oceanic to continental subduction and the topographic consequences of the progressive slowdown of the convergence rate during continental subduction. Tunini et al. (2015) applied a 2-D FEM model combining geophysical-petrological methodology in order to study the thermal, compositional, density and seismological structure of the crust and upper mantle along two transect across the Arabia-Eurasia collision region.

In this thesis we used the 2-D FEM methodology in order to investigate both inter-seismic and co-seismic deformation related to the MFT along the 2-D geological model presented in chapter 3 (Figure 10). The chosen software was Marc software (MSC Software Corporation) of which the first commercial version is available since 1972. Here it is possible to set up the contact type between two different surfaces (faults on our instance) and boundary conditions.

The pre-build 2-D geological model (Figure 10) was divided into three homogeneous domains, to which values of Young's modulus, Poisson's ratio and density were assigned considering an elastic rheology (Table 2). The friction coefficient was set as $\mu = 0.6$ (Byerlee, 1967; 1978) for the contact (MFT on our instance). The model was divided into 14,314 quadrilateral element and 15,298 nodes. Near faults, homogeneous zone boundaries and top surface, the sides of each single

quadrilateral element are about 1 km long, increasing in size away from contacts (Basilici et al., 2020b).

Domain	Formation or Group	Lithology	Young's modulus (Pa)	Poisson's ratio	Density (Kg/m^3)
Arabian cover	Foredeep infill Asmari, Shabazan, Ilam, Sarvak, Garau, S-N-B, Sehkaniyan, Sarki, Baluti, Kurre Chine, Geli Khana, Beduh, Mirga Mir – Chia Zairi	sandstone limestone and shale	3.62E+10	0.23	2.55E+03
Arabian basement	basement	granite	6.00E+10	0.22	2.80E+03
Sanandaj-Sirjan Zone	volcanic arc	volcanic rock	5.16E+10	0.25	2.80E+03

Table 2 – Parameter values used in the FEM model (Basilici et al., 2020b). Density values are from Teknik et al. (2019; also used in Basilici et al., 2019; 2020a). Values of Young's modulus and Poisson ratio were defined according to previous FEM models by Zhao et al. (2004) and Zhu and Zhang (2013). Formations and groups belonging to the Arabian sedimentary cover are from Tavani et al. (2018a).

Numerical modelling included two independent FEM simulation carried out using the same mesh: a first procedure was used to investigate surface vertical motions associated with the MFT co-seismic stage by modelling the characteristic earthquake, while a second procedure was used to analyse inter-seismic stress and strain accumulation (Basilici et al., 2020b). A sensitivity analysis was carried out in order to quantify the impact of variations of density values and Young's modulus. Varying the density from 2.7E+03 to 2.9E+03 kg/m^3 (Basilici et al., 2019; 2020a; Teknik et al., 2019), and Young's modulus from 4.5E+10 to 5.5E+10 Pa in the Sanandaj-Sirjan Zone and from 5.5E+10 to 6.5E+10 Pa in the basement (Zhao et al., 2004; Zhu and Zhang, 2012) we obtained uncertainties always smaller than 4%. In particular, the uncertainty

varies nonlinearly along the cross-section M-M' for Young's modulus variations within the previously specified ranges, with a mean value of 2% for the central zone of the transect (175 – 225 km in Figure 10). On the other hand, the uncertainty is almost constant in the case of the density, with a maximum value of 3.7% (Basilici et al., 2020b).

5.2 – Co-Seismic Simulation

To produce a realistic simulation of a co-seismic phase of a fault, we need to select the characteristic earthquake that identifies a seismic cycle. In Figure 21 are shown earthquakes with $M_w \geq 5.5$ recorded from 1967 to the present day in western Lurestan.

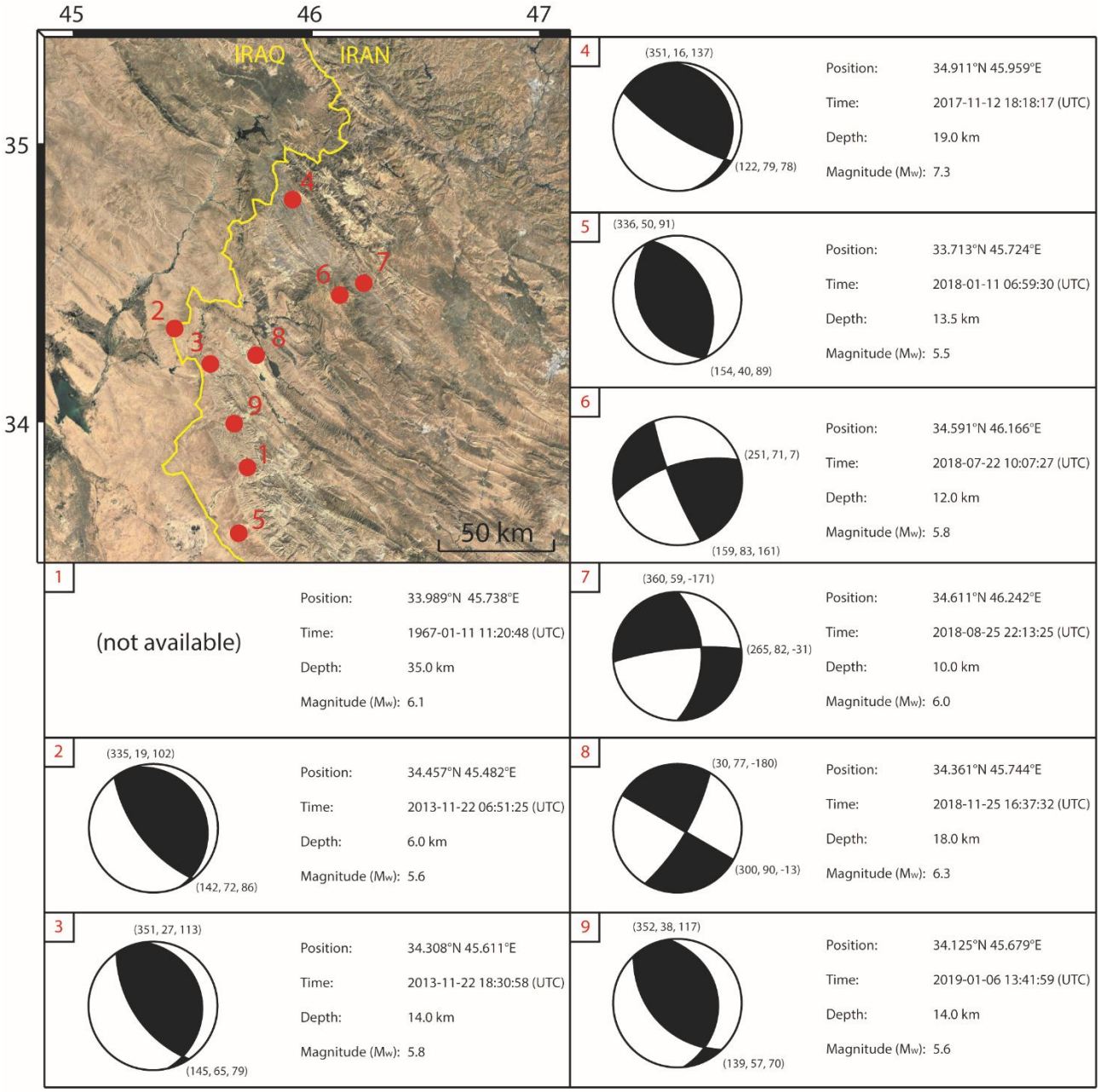

Figure 21 (modified from Basilici et al., 2020b) – Earthquakes with $M_w \geq 5.5$ recorded from 1967 to the present day in western Lurestan. Epicentral location, event location, magnitude and fault plane solutions are from USGS catalogue (https://earthquake.usgs.gov/earthquakes/search/ ; last access: 06 October 2020).

The November 12, 2017, Mw = 7.3 earthquake was selected as the characteristic earthquake (i.e. a seismic event rupturing the entire fault) to investigate the behaviour of the MFT. Data on the recurrence interval of similar large-magnitude events nucleated along the MFT are not available, as catalogue data from the study area start from 1967 (Basilici et al., 2020b).

Modelling of the co-seismic stage was divided into two different steps (Figure 22). The first step consisted in setting the boundary conditions of the model, so as to observe the effects of gravity alone, it allows the achievement of "equilibrium conditions" between gravity, hydrostatic pressure of the Earth's mantle, and compaction of rocks and contacts. The boundary conditions of the model were the following:

1. The surface was free to move in all direction.
2. The SW and NE boundary were locked in the horizontal direction and free to move in the vertical directions.
3. The base was treated as a Winkler's foundation (Williams and Richardson, 1991). This model base was used to simulate hydrostatic pressure of the Earth's mantle: free horizontal movement was allowed and vertical motion was controlled by an elastic spring with stiffness coefficient K equal to $K = \frac{A}{L}E$, where A is the base length, L is the thickness of the model and E is the average of Young's modulus of the rocks included in the model.

The second step, implemented in succession, consisted in the sudden movement of a part of the fault plane, in order to simulate stick-slip behaviour. It considers free to move (by stick-slip) a portion of the fault located at a depth between 14 and 20 km, with a total slip of 4 m (as inferred for the November 12, 2017 earthquake; Vajedian et al., 2018). This procedure allowed us to compute the surface motion in the vertical direction (Basilici et al., 2020b).

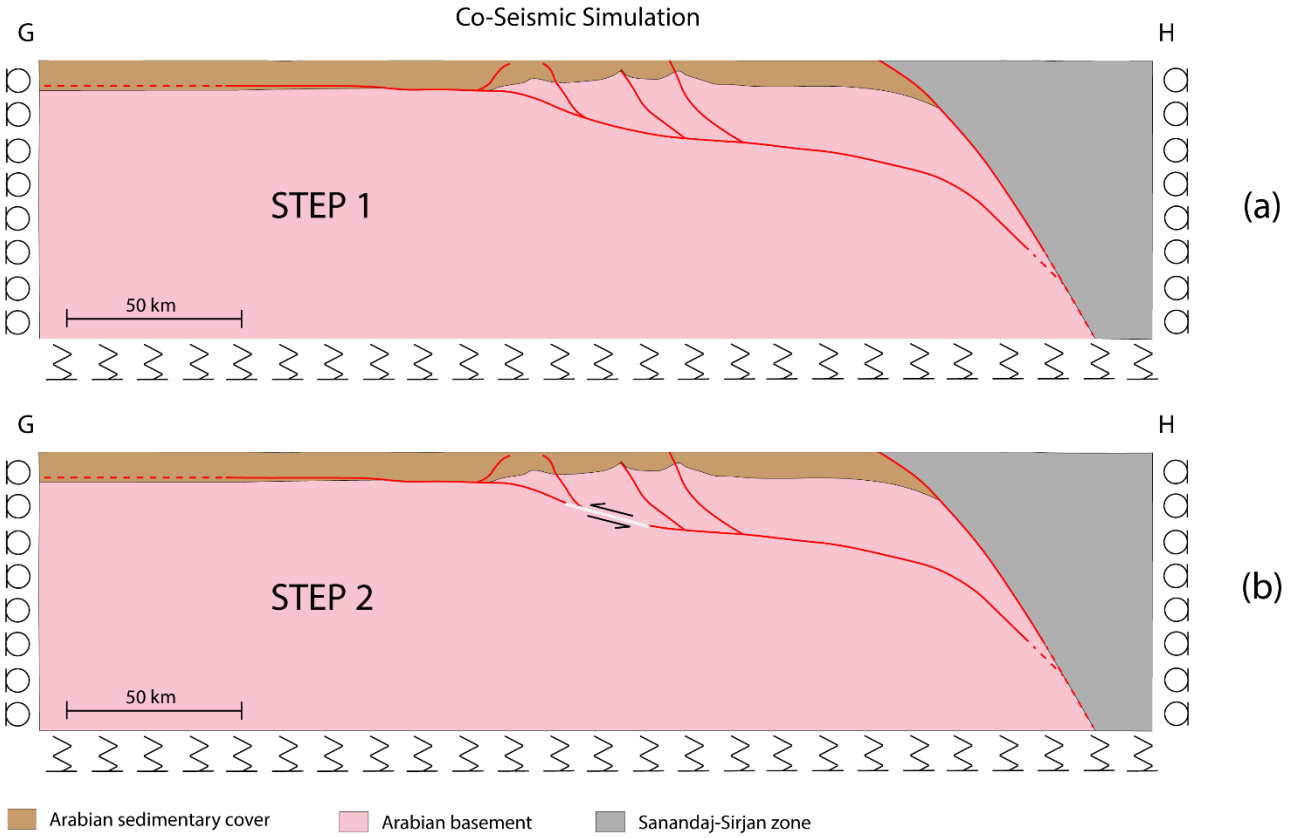

Figure 22 (modified from Basilici et al., 2020b) – Geometry and boundary conditions for the co-seismic simulation. (a) Step 1: the surface is free to move in all directions under the influence of gravity (applied as volumetric force on each elementary component), while the lateral boundaries are locked in the horizontal direction and the base of the model is treated as a Winkler's foundation (William and Richardson, 1991). (b) Step 2: the boundary conditions are the same as those for step 1, but the fault portion coloured in white is let free to move instantaneously, while the rest of the fault (coloured in red) is locked.

5.3 – Inter-Seismic Simulation

The inter-seismic simulation was used to analyse inter-seismic stress and strain accumulations. It shares the first step with the co-seismic simulation procedure, however, in this case, the second step consisted of the horizontal movement of the SW boundary towards the NE boundary, in order to simulate observed movements constrained by the GPS stations located at the surface (Figure 23, Basilici et al., 2020b).

The unique GPS data available in our study area are those recorded by the Ilam station (Vernant et al., 2004) for the period 1999-2001. The related velocity projected along our model section results in a value of 2.3 ± 1 mm yr^{-1} towards the NE,

considering a fixed Central Iranian Block (Sanandaj-Sirjan Zone) reference frame. Therefore, the motion of the SW boundary during the second step was set up to move Ne-ward with a horizontal velocity of 2.3 mm yr^{-1} in correspondence with the projected position of the Ilam GPS station in the model. The second step involves keeping the seismogenic MFT patch locked (this is the fault that is inferred to have slipped during the November 12, 2017 earthquake; Gombert et al., 2019; Nissen et al., 2019), together with the upper crustal fault splays branching out from the upper portion of the main MFT. On the other hand, the deeper (NE) portion of the MFT was let free to move (by stable sliding), thus simulating a creeping detachment in the middle to lower crust (Basilici et al., 2020b).

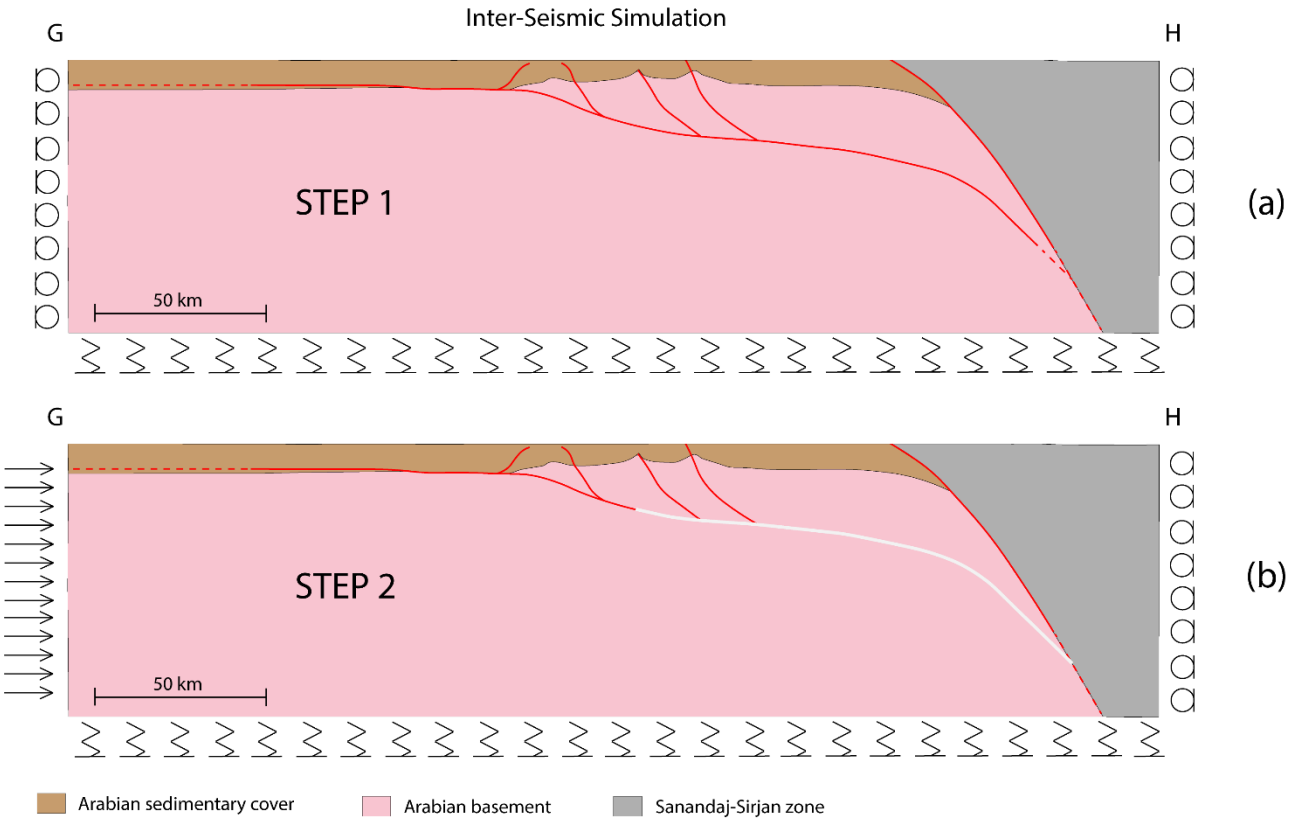

Figure 23 (modified from Basilici et al., 2020b) – Geometry and boundary conditions for the inter-seismic simulation. (a) Step 1: the surface is free to move in all directions under the influence of gravity (applied as volumetric force on each elementary component), while the lateral boundaries are locked in the horizontal direction and the base of the model is treated as a Winkler's foundation (William and Richardson, 1991). (b) Step 2: a horizontal NE-ward velocity of 2.3 mm yr^{-1} is introduced in correspondence of the projected position of the Ilam GPS station. The fault portion coloured in white is that let free to move by stable sliding, while the rest of the fault (coloured in red) is locked.

This procedure allowed us to compute the amount of equivalent Von Mises stress (σ_{VM}):

$$\sigma_{VM} = \sqrt{\frac{3}{2}\left(\sum_{ij}\sigma'_{ij}\,\sigma'_{ij}\right)}, \text{ with } \sigma'_{ij} = \sigma_{ij} - \frac{1}{3}\sum_{k}\delta_{ij}\sigma_{kk} \quad (27)$$

where σ_{ij} is the stress component and δ_{ij} is the Kronecker delta, of equivalent (Von Mises) strain (ε_{eq}):

$$\varepsilon_{eq} = \sqrt{\frac{3}{2}\left(\sum_{ij}\varepsilon'_{ij}\,\varepsilon'_{ij}\right)}, \text{ with } \varepsilon'_{ij} = \varepsilon_{ij} - \frac{1}{3}\sum_{k}\delta_{ij}\sigma_{kk} \quad (28)$$

where ε_{ij} is the strain component (Zhuang et al., 2019), and of surface motion in the vertical direction, accumulated in a given time interval during the inter-seismic stage. The calculation procedure was set up to cover a period of 1000 years in order to reach appreciable values of accumulated stress, strain and surface displacement.

5.4 – Structural FEM Model Results

The values of resulting vertical surface displacement for co-seismic scenario is shown in Figure 24. The modelled hypothesis of a characteristic earthquake of M_w = 7.3 yields curves of vertical surface displacement (Figure 24) is characterized by two peaks. The first peak is positive and shows an increment from 0 to 1.2 m at a distance around 162 km, while the second peak is negative and shows a decrement to -0.4 m at ca. 190 km. These values are in very good agreement with the results of the analysis of geodetic data obtained by Feng et al. (2018) relative to the November 12, 2017 Iran-Iraq earthquake, which pointed out an uplift of ca. 1 m in the same area and a

subsidence of the zone immediately to the NE of 0.4 m (Basilici et al., 2020b). The values of resulting vertical surface displacement, total strain and equivalent of Von Mises stress for inter-seismic scenario is shown in Figure 26.

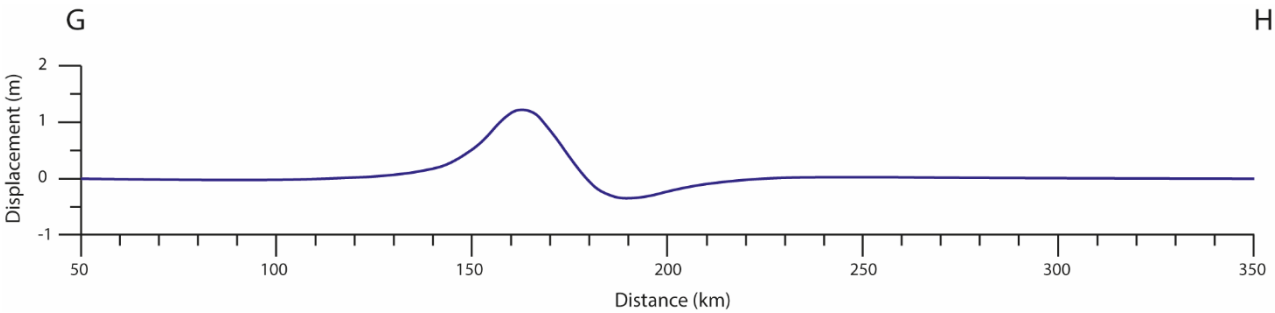

Figure 24 (modified from Basilici et al., 2020b) – Output of the FEM showing vertical surface displacement for the co-seismic stage (characteristic earthquake of M_w = 7.3).

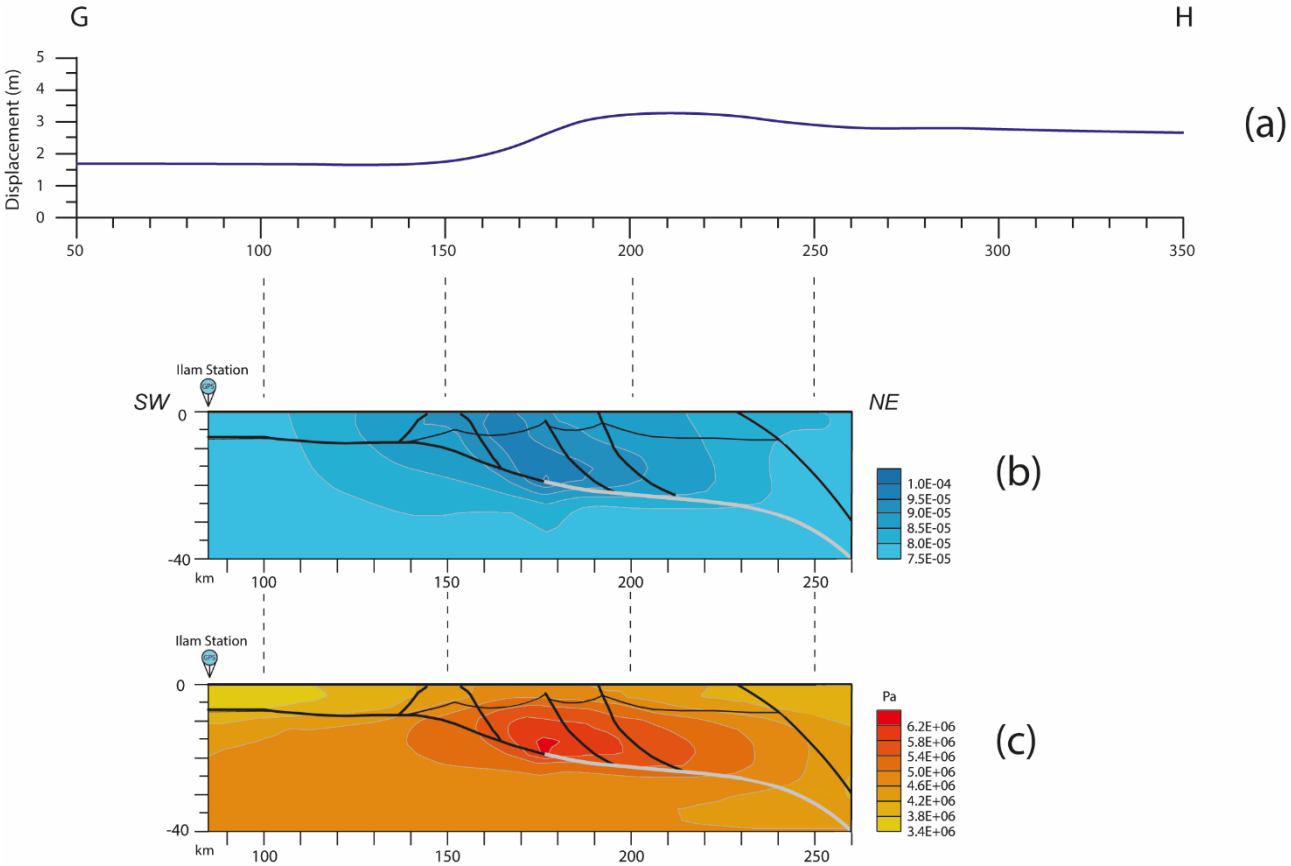

Figure 25 (modified from Basilici et al., 2020b) – Output of the FEM showing: (a) vertical surface displacement for the inter-seismic stage (1000 years), (b) equivalent strain and (c) equivalent Von Mises stress for the inter-seismic stage (zoom of the central part of the modelled section). Black fault segments are locked, whereas white fault segments are unlocked (i.e. free to slip by stable sliding).

The model output of vertical displacement for the inter-seismic stage (integrated over a 1000 years time span) is characterized by a plateau in the SW part of the model, increasing from 150 km NE-ward to define a wide bulge between 190 and 240 km and then gently decreasing to the NE (Figure 25a). A zone of maximum resulting total strain occurs in the hanging wall of the MFT (Figure 25b), above the deeper portion of the seismogenic detachment segment. This region of maximum deformation is comprised between the Sheykh Saleh Fault to the NE and the Miringeh Fault to the SW, being located just NE of the November 12, 2017 earthquake hypocentre. This latter falls anyway in a zone of relatively high strain (in the range of 9.0E-05 to 9.5E-05). It is worth noting that the zone of marked strain accumulation reaches the surface, maintaining similar values to those characterizing the locked detachment at depth. The accumulated strain decreases gradually both NE-ward and SW-ward, defining a ca. 140 km wide perturbed area. The Von Mises stress (Figure 25c), besides displaying an expected peak (exceeding a value of 6.2E+06Pa) at the junction between creeping and locked detachment segments, is characterized by roughly elliptical, concentric regions of high stress elongated in a sub-horizontal direction. Stress accumulation at the surface is not as marked as that occurring at depth (particularly in the 10-20 km range), as stress diffusion appears to follow a horizontal preferential direction. As a matter of fact, the perturbed (stressed) region exceeds 175 km in the horizontal direction (Basilici et al., 2020b).

6 – Discussion

6.1 – Geothermal Model

During last years, new modelling methods and software have been developed allowing us to investigate a geologically complex structure as the "Main Frontal Thrust" of the Lurestan region, Zagros thrust belt (Iran). GPS measurements show that the northward relative motion of the Arabian Plate is still active today, with oblique convergence occurring at a rate of ca. 2 cm/yr with respect to fixed Eurasia. Our purpose was to reconstruct a 2-D and 3-D geothermal models of the Lurestan arc and to provide thermal constraints.

To reach our aim, we compared the resulting 2-D model (Figure 16) with the numerical results obtained by previous studies (Kargaran and Neubauer, 2015; Shekarifard et al., 2012; Tunini et al., 2015; Vernant and Chéry, 2006) to improve the description of the thermal structure of Lurestan sector (Figure 26). Figure 26a shows how an increment of Q_m (from 20 to 25 mW/m^2) produced a shift of the Q_s curve without changing its shape. Both curves remain within the range of 40 – 80 mW/m^2, which is consistent with recent studies by Shekarifard et al. (2012) and by Kargaran and Neubauer (2015), but Q_s values obtained in this study display a marked variation with respect to published results by Kargaran and Neubauer (2015), it passes from lower values in the foreland and thrust front region to higher values in the thrust belt interior. The Q_s curve obtained for a (Q_m) = 20 mW/m^2 provides a better fit as compared with results by Kargaran and Neubauer (2015), in particular, a value congruency of about 61 mW/m^2 is met for pseudo-well 4, while a minor difference occurs for pseudo-well 5. The Q_s curve obtained for a (Q_m) = 25 mW/m^2 shows a congruency in correspondence of pseudo-well 3, but displays a larger difference towards thrust belt interior.

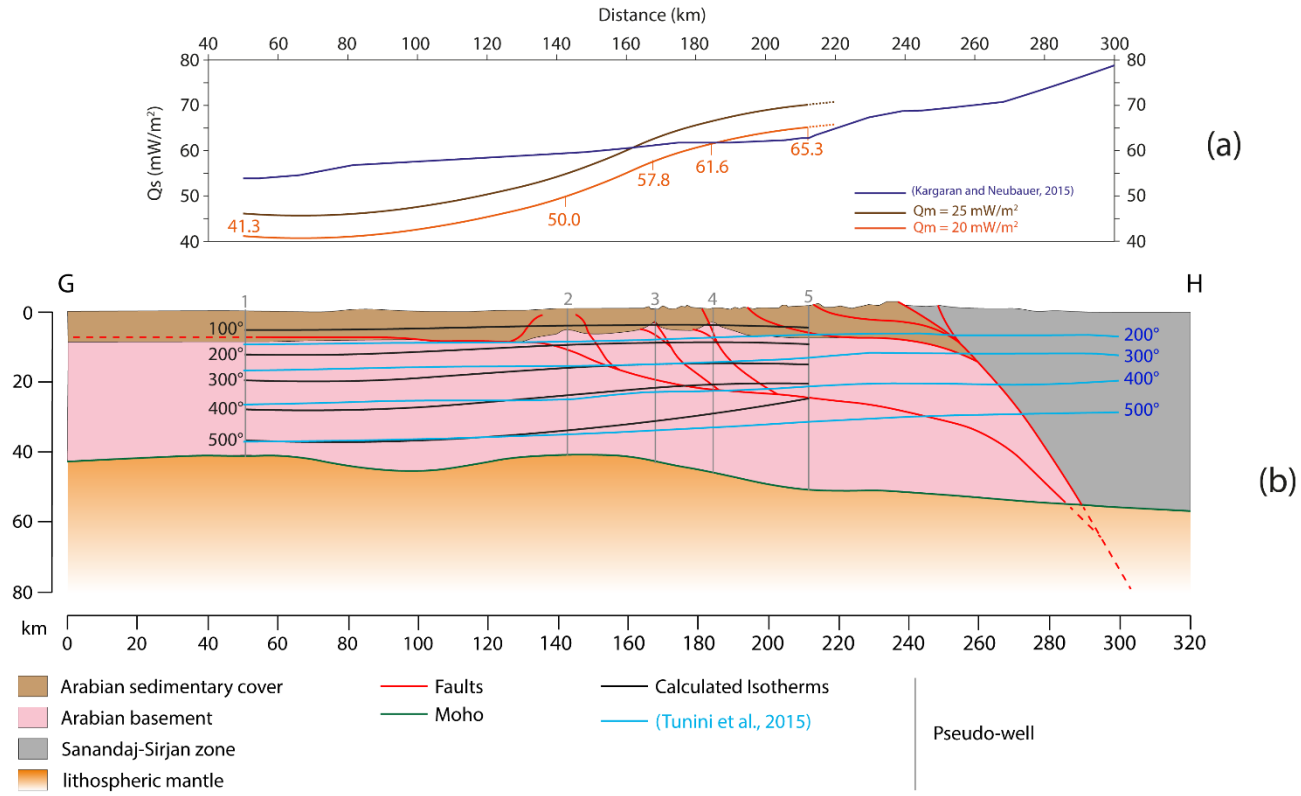

Figure 26 – (a) Surface heat flow (Q_s) for a (Q_m) = 20 mW/m^2 and (Q_m) = 25 mW/m^2 compared with Kargaran and Neubauer (2015) curve. (b) 2-D thermal structure of the Zagros thrust belt for a (Q_m) = 20 mW/m^2 compared with the isotherms by Tunini et al. (2015; modified from Basilici et al., 2019).

Figure 26b shows how our temperature isolines are generally consistent with those obtained by Tunini et al. (2015), a part for some difference that occurs in the thrust belt interior. The trend of our results is in good agreement with the trend obtained by Vernant and Chéry (2006; Basilici et al. 2019). Isotherms contour maps obtained by spline interpolation (Figure 20) allowed us to produce a 3-D model of the thermal structure of the Lurestan arc subsurface (Figure 27).

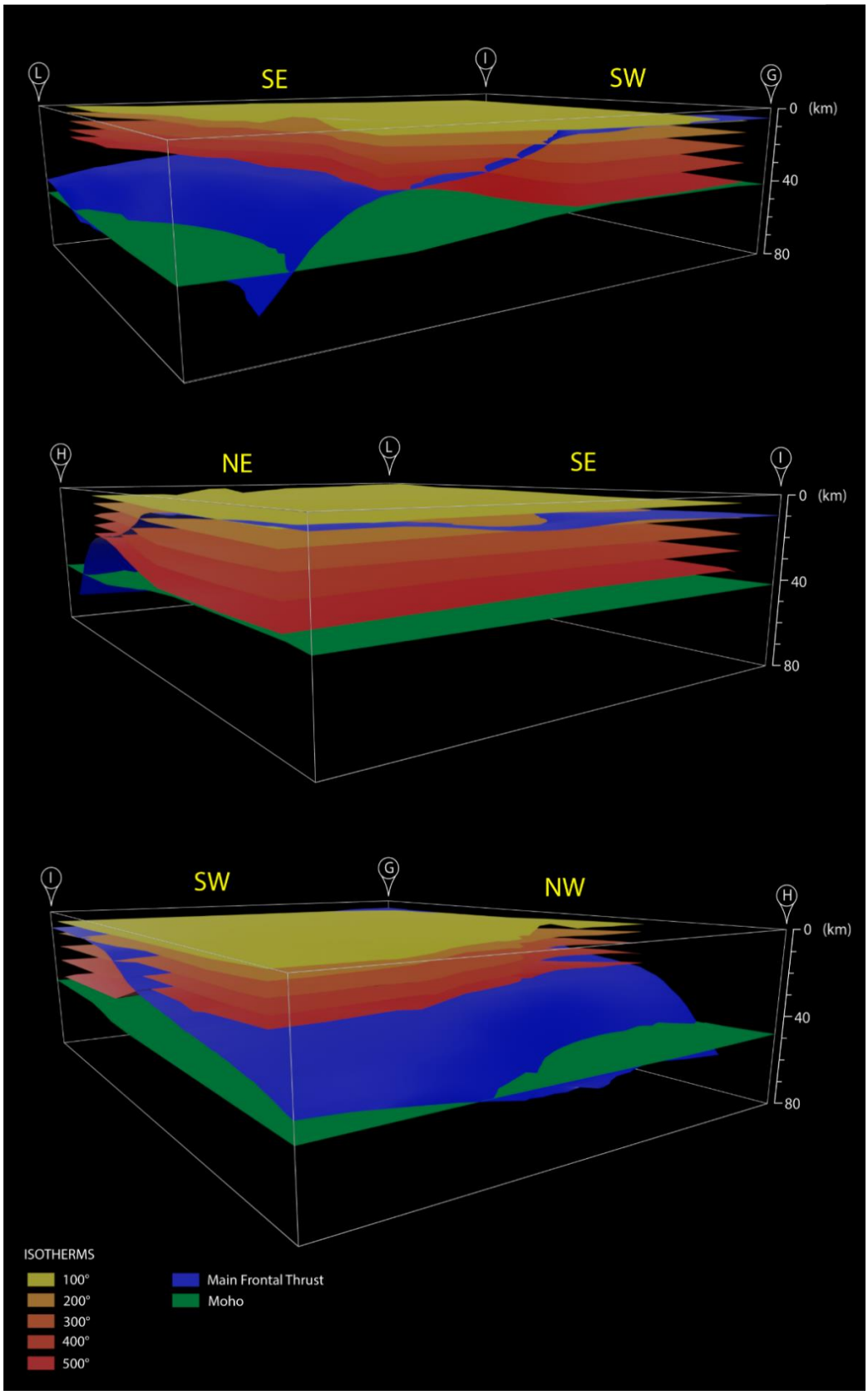

Figure 27 – Three different views of the 3-D thermal model. The model shows isotherms obtained using spline interpolation for the 100 – 500 °C temperature range (100°C steps), together with the MFT and the Moho, this last was calculated by Jiménez-Munt et al., (2012; modified from Basilici et al., 2020b).

The 3-D model of the thermal structure of the Lurestan arc (Figure 27) shows a good fit with the thermal structure obtained by second-order power-law polynomial interpolation (Figure 28), thus confirming the consistency and robustness of the thermal structure 3-D model (Basilici et al., 2020b).

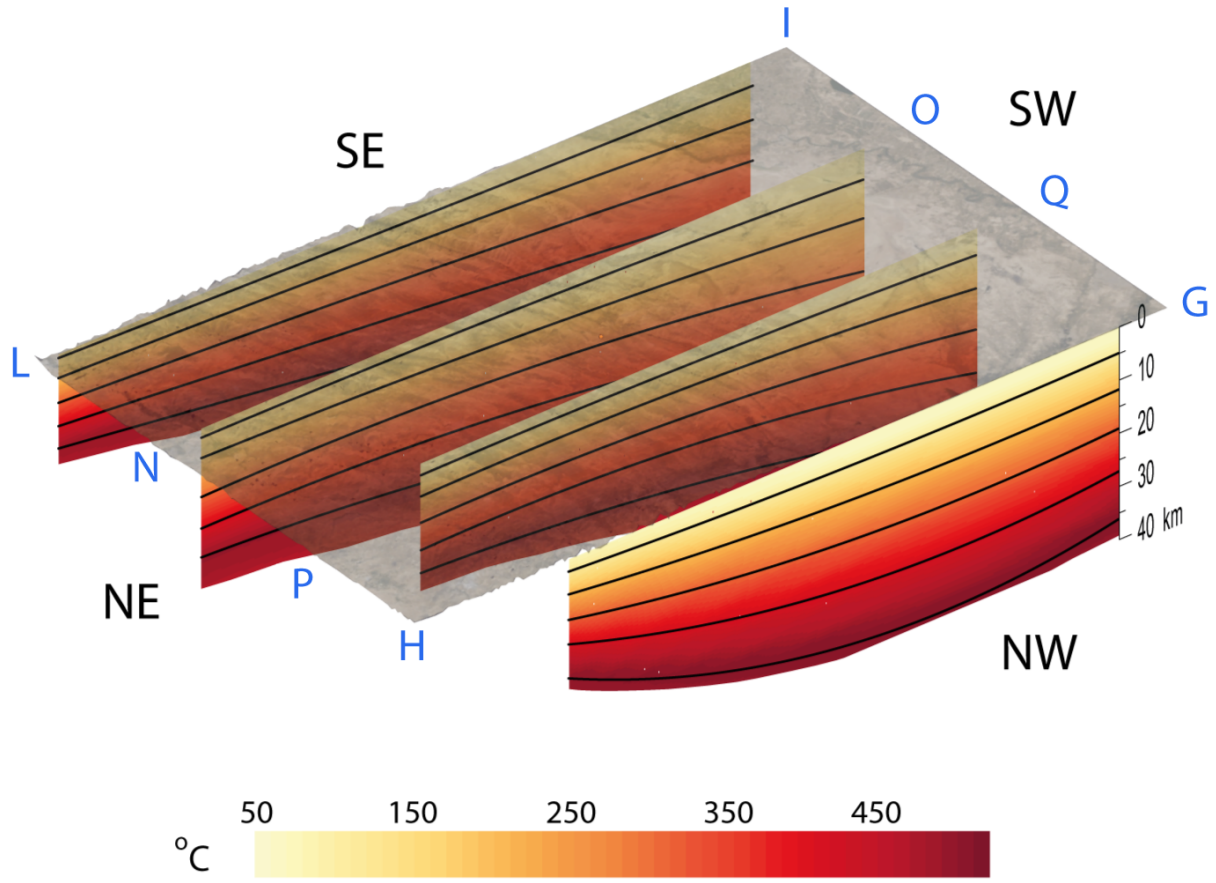

Figure 28 – Thermal structure of the Lurestan arc as defined by isotherms calculated using a second-order power-law polynomial interpolation along cross-sections HG, PQ, NO and LI (located in Figure 19; black lines are 100, 200, 300, 400 and 500°C isotherms). Surface topography is from the 30 m resolution ASTER GDEM (modified from Basilici et al., 2020b).

The 3-D model of the thermal structure (Figure 27) shows how isotherms are characterized by a general SW-ward deepening, which clearly outline a higher temperature axial zone of the mountain belt. On the other hand a “colder” zone is present in the outer zone of the SFB and the adjacent foreland, there, the widely spaced

isotherm pattern gives way to a pattern characterized by progressively more densely spaced isotherms, which become closer to each other moving to the SE portion of the Lurestan arc. The NE-ward temperature increment was due to crustal thickening associated with the thrust, as the NE dipping MFT produces a progressively increasing amount of basement offset by the fault (Δ_z). Also, this along-strike, SE-ward temperature increase was controlled by the 3-D geometry of the MFT, which is characterized by a low-angle crustal ramp in its SE portion, changing to a steep ramp rapidly reaching lower crustal depths to the NW. The resulting thermal structure tended to mimic the general arc-shape geometry of the mountain belt, as readily observable by comparing the isotherm depth contours with the trace of the MFT in Figure 20. The junction between the Lurestan arc and the Kirkuk embayment also was clearly reflected by the crustal thermal structure. Therefore, the geometry of the MFT shows a clear correlation with the thermal structure of the area (Basilici et al., 2020b).

Tavani et al. (2020) concluded that the sinusoidal shape of the MFT and its different position in the Kirkuk embayment and Lurestan arc was promoted by lateral segmentation of the Jurassic rift accommodated by transfer faults. Despite this long-lived paleo-tectonic control and the fundamental role of structural inheritance, the development of the MFT and its activity controlling it. Therefore, late-stage crustal ramp-dominated thrusting (Butler and Mazzoli, 2006) not only led to the development of a prominent geomorphological boundary between the high Zagros mountains and the low foothills to the SW but also appears to have exerted a strong control on the thermal structure of the entire Lurestan arc (Basilici et al., 2020b).

6.2 – Structural Model

The results of finite element modelling (FEM), including predicted uplift pattern and rate along the analysed crustal section, are compared with a tectonic geomorphology analysis in order to unravel the most reliable tectonic scenario for the active tectonic setting of the study area.

To produce a cumulative vertical surface displacement curve, we integrated the calculated vertical surface displacement of both co-seismic and inter-seismic stages over a time span of 1000 years (Figure 29). As a data on the recurrence interval of the characteristic earthquake are not available, the reasonable hypothesis of a characteristic earthquake occurring every 1000 ± 500 years on average has been adopted (Basilici et al., 2020a).

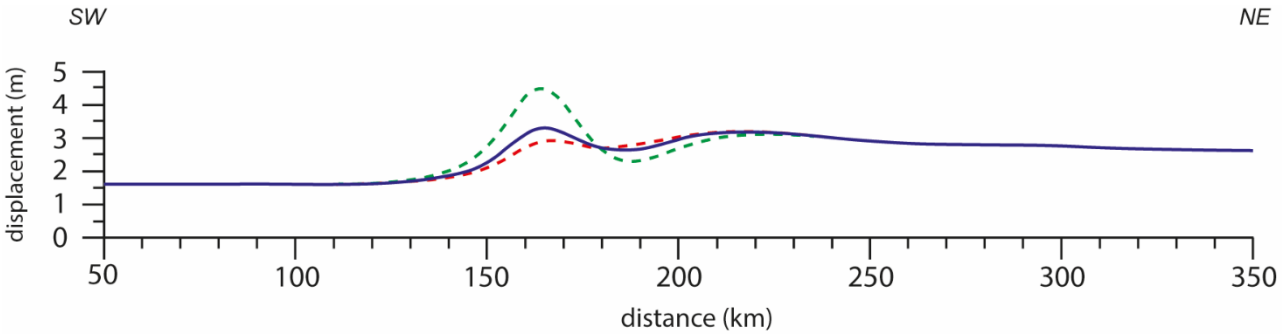

Figure 29 – Cumulative vertical surface displacement along the trace of cross-section GH integrated over a time span of 1000 years (modified from Basilici et al., 2020a). It resulting from the sum of co-seismic and inter-seismic stages considering a characteristic earthquake recurrence interval of 1000 years (blue line); 500 years (green dashed line); and 1500 years (red dashed line).

To improve the description of the rock uplift, we compared the resulting cumulative vertical surface displacement (Figure 29) with an investigation of the large-scale features of topography provided by Basilici et al. (2020a) on the same trace GH of the 2-D geological model (Figure 10). The geomorphology analysis was inferred from the qualitative and quantitative analyses of the features of the landscape and drainage network carried out using a Digital Elevation Model (the 30 m resolution ASTER GDEM), satellite images (Google Earth, 2019) and orthophotos, and a GIS-based analysis of the DEM. The qualitative analysis of the topography was aimed at collecting information that could allow identifying the contribution exerted by variable

erodibility of outcropping rocks vs. surface motions in the formation of the landscape. This included an analysis of the active and relic drainage network, carried out through, e.g. identification and mapping of abandoned fluvial paths and point of capture, and of erosional and depositional landforms suggestive of a multi-stage development of the relief. Quantitative constraints to the features of the relief were obtained from the analyses of the spatial distribution of elevation and local relief and from river longitudinal profiles. The elevation parameter depends on both resistance to weathering of outcropping rocks and uplift. However, the maximum elevation is considered as primarily influenced by resistance to erosion of outcropping rocks, while the mean elevation is considered as more closely representing a response to surface uplift (England and Molnar, 1990). On the other hand, the local relief is considered a robust indicator of uplift, particularly in regions underlain by rocks with rather homogeneous resistance to erosion (DiBiase et al., 2010). The elevation and local relief were analysed both along a profile and in map view. A swath profile was constructed following the methodology of Perez-Peña et al. (2017) along a 320 km long and 40 km wide transect centered on the trace of the 2-D geological model (Basilici et al., 2020a).

In Figure 30 is shown the spatial distribution of topography features compared with the cumulative vertical surface displacement of Figure 29.

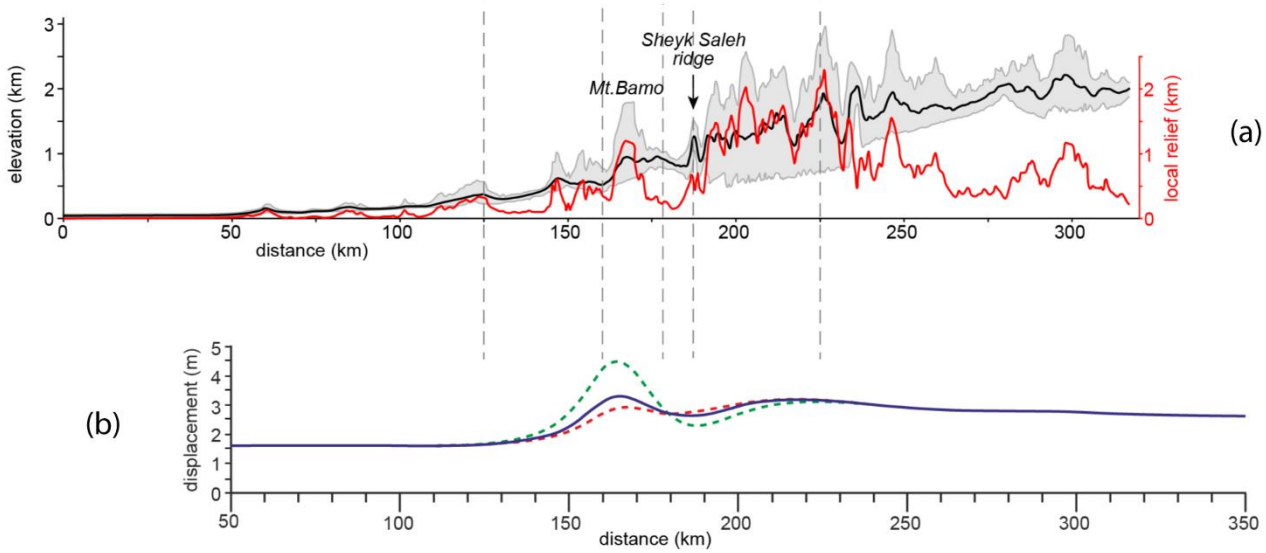

Figure 30 – (a) Spatial distribution of topography features. The red line is the local relief, the black line is the elevation along the transect and the grey zone represents the spatial distribution of elevation into the 40 km wide transect. (b) Cumulative vertical surface displacement along the trace of cross-section GH integrated over a time span of 1000 years (modified from Basilici et al., 2020a). It resulting from the sum of co-seismic and inter-seismic stages considering a characteristic earthquake recurrence interval of 1000 years (blue line); 500 years (green dashed line); and 1500 years (red dashed line).

It is worth noting that the uncertainty involved in the extrapolation of co-seismic displacements over a 1000 years period is not a major issue in this context, as our focus is on the definition of the position of areas of major surface deformation rather than on the absolute value of vertical displacement in Figure 29). Within this framework, a likely contribution of post-seismic afterslip taking place during years or even decades following the main shock (Copley, 2014; Copley and Reynolds, 2014) would also be taken into account by our modelling of surface displacement, assuming slip occurred along the same thrust originating the earthquake. A different issue is that the reference timescale of the FEM (10^2 – 10^3 years) differs by one – two orders of magnitude from that involved in the construction of modern topography (106 years; Whipple, 2001). Nevertheless, the modelled seismic behaviour of the MFT provide useful insights into the source of the late part of the surface displacement recorded by topographic features

and river network, also allowing one to infer whether one or more structures are contributing to such a displacement. Our results show that the local high relief in correspondence of the Mt. Bamo (Figure 30) also occurs in the region of maximum accumulated strain, which reaches shallow depths according to FEM of inter-seismic deformation (Figure 25b). At ca. 215 km, a further maximum of vertical displacement in the model occurs, the uplift decreasing then slightly to the NE (Figure 29). Overall, this entire area of the model defines an uplifted crustal block in the hanging wall of the mid crustal, gently dipping segment of MFT. The vertical surface motion pattern of Figure 29 results from rather distinct contributions provided by continuous regional uplift characterising inter-seismic stages and focused deformation in the area of the Mt. Bamo associated with co-seismic displacement.

Therefore, our FEM suggests that the Quaternary development of the relief defining the MFT is mainly related to the co-seismic deformation, while generalized uplift of the orogen segment located more to the NE is associated with stable sliding along the deeper portions of the MFT. Consistent with results of numerical modelling of topography growing over seismically active blind thrusts (Ellis and Densmore, 2006), the two uplifted areas are separated by a belt characterized by co-seismic subsidence associated with the large earthquake ($M_w > 7$) occurring in the region (Basilici et al., 2020a).

7 – Conclusions

This thesis provides, for the first time, a comprehensive picture of the thermal structure of the Zagros fold and thrust belt calculated using an analytical procedure. It resulted in 2-D and 3-D models that emphasize the major role played by a crustal thrust fault (MFT) in controlling the thermal structure of the region, a very good correlation between high temperature gradients in the crust and the amount of basement offset by the MFT testified it. The study area presents a zone of relatively high geothermal gradient due to the marked effect of recent (Pliocene) thick-skinned inversion and associated basement thrusting, this could have interesting implications in terms of geothermal energy potential (Basilici et al., 2019, 2020b).

The structural finite element modelling presented in this thesis shows how the vertical surface displacement is the result of a combination of slip accumulated during large ($M_w > 7$) seismic events and continuous displacement along a gently dipping, mid crustal thrust detachment. Co-seismic and inter-seismic stages models allowed us to gain new insights into the relative contribution of each process in the development of the relief: while inter-seismic deformation produces a generalized uplift of the whole crustal block in the hanging wall of the mid crustal segment of the major thrust detachment, co-seismic displacement controls localized uplift of a distinct topographic feature located above the main upper crustal ramp of the same major thrust fault (Basilici et al., 2020a).

The resulted information provided by this thesis is of pivotal importance for any quantitative modelling of the tectonic behaviour of this actively deforming Iran sector, geodynamic studies, as well as in geothermal/hydrocarbon exploration. It may also have important implications for active tectonic studies and seismotectonic modelling in an area recently affected by a $M_w > 7$ earthquake.

We explained, in this thesis, how the MFT interacts with the entire Lurestan arc in terms of thermal structure and active deformation. The used mathematical approach, analytical for the thermal modelling and numerical for the structural modelling, is able to realize exhaustive 2-D and 3-D models. A similar approach can be used to study thrust zones in other locations of the world. Santini et al. (2020) applied a similar analytical procedure to the outer Albanides and adjacent Adriatic crustal sector (Albania) to calculate surface heat flow, geotherms and isotherms in an area affected by a strong earthquake (M_w = 6.2) during November 2019. The authors observed a thermal structure strongly influenced by frictional heating produced by faults, similarly to Zagros thrust belt.

The FEM method is growing during this years, new powerful softwares are now in development phase. Thanks to modern technologies, numerical procedures will be applied, next years, to the 3-D geological models and will be capable to give a better explanation of the fault activity-active deformation relationship.

To improve this work, studies will be realized in future. We will work to develop a 3-D FEM modelling using the 3-D geological model (Figure 12) as a base. The 3-D numerical procedure will be capable of showing the activity of the MFT for its entire fault's surface and to highlight the active deformation in a 3-D view, observing the surface vertical displacement in the map, we will explain how inter-seismic and co-seismic displacements control uplift of distinct topographic feature in the entire Lurestan arc. A 3-D geological model will be realized in Albania, to improve, subsequently, a structural 3-D FEM to understand outer Albanides active deformation and to observe how co-seismic and inter-seismic displacements control the development of the mountain chain relief.

8 – References

Agard, P., Omrani, J., Jolivet, L., Mouthereau, F. Convergence history across Zagros (Iran): Constraints from collisional and earlier deformation. *International Journal of Earth Sciences* **2005**, 94, 401-419. doi:10.1007/s00531-005-0481-4

Agard, P., Omrani, J., Jolivet, L., Whitechurch, H., Vrielynck, B., Spakman, W., Monié, P., Meyer, B., and Wortel, R. Zagros orogeny: A subduction-dominated process. *Geological Magazine* **2011**, 148, 692–725. doi:10.1017/S001675681100046X

Alavi, M. Tectonics of the Zagros orogenic belt of Iran: new data and interpretations. *Tectonophysics* **1994**, 229, 211-38. doi:10.1016/0040-1951(94)90030-2

Alavi, M. Structures of the Zagros Fold-Thrust belt in Iran. *American Journal of Science* **2007**, 307, 1064-1095. doi:10.2475/09.2007.02

Allen, M., Jackson, J., Walker, R. Late Cenozoic reorganization of the Arabia-Eurasia collision and the comparison of short-term deformation rates. *Tectonics* **2004**, 23, TC2008. doi:10.1029/2003TC001530

Allen, M. B., Kheirkhah, M., Emami, M. H. and Jones, S. J. Right-lateral shear across Iran and Kinematic change in the Arabia-Eurasia collision zone. *Geophysical Journal International* **2011**, 184, 555-574. doi:10.1111/j.1365-246X.2010.04874.x

Austermann, J. and Iaffaldano, G. The role of the Zagros orogeny in slowing down Arabia-Eurasia convergence since ~5 Ma. *Tectonics* **2013**, 32, 351-363. doi:10.1002/tect.20027, 2013

Authemayou, C., Chardon, D., Bellier, O., Malekzadeh, Z., Shabanian, E., Abbassi, M. R. Late Cenozoic partitioning of oblique plate convergence in the Zagros fold-and-thrust belt (Iran). *Tectonics* **2006**, 25, TC3002. doi:10.1029/2005TC001860

Baharifar, A., Moinevaziri, H., Bellon, H., Pique, A. The crystalline complexes of Hamadan (Sanandaj-Sirjan zone, western Iran): Metasedimentary Mesozoic sequences affected by Late Cretaceous tectono-metamorphic and plutonic events. *Comptes Rendus Geoscience* **2004**, 336, 257-82. doi: 10.1016/j.crte.2004.09.014

Bahroudi, A. and Talbot, C. J. The configuration of the basement beneath the Zagros Basin. *Journal of Petroleum Geology* **2006**, 26(3), 257-282. doi:10.1111/j.1747-5457.2003.tb00030.x

Basilici, M., Mazzoli, S., Megna, A., Santini, S., Tavani, S. Geothermal Model of the Shallow Crustal Structure across the "Mountain Front Fault" in Western Lurestan, Zagros Thrust Belt, Iran. *Geosciences* **2019**, 13(9), 2140. doi:10.3390/en13092140

Basilici, M., Ascione, A., Megna, A., Santini, S., Tavani, S., Valente, E., Mazzoli, S. Active deformation and relief evolution in the western Lurestan region of the Zagros mountain belt: new insights from tectonic geomorphology analysis and finite element modeling. *Tectonics* **2020a**, 39(12), e2020TC006402. doi: 10.1029/2020TC006402

Basilici, M., Mazzoli, S., Megna, A., Santini, S., Tavani, S. 3-D Geothermal Model of the Lurestan Sector of the Zagros Thrust Belt, Iran. *Energies* **2020b**, 13(9), 2140. doi:10.3390/en13092140

Berberian, M. First Seismotectonic Map of Iran, scale 1:2,500,000. In: Contribution to the Seismotectonic of Iran, Part II. First Edition. *Geological Survey of Iran* **1976**.

Berberian, F. and Berberian, M. Tectono-Plutonic Episodes in Iran. In: Zagros-Hindu Kush-Himalaya Geodynamic Evolution. Gupta, H.K. and Delany, F.M. eds. *Geodynamics Series* **1981**, American Geophysical Union, Washington DC, 3, 5-32.

Berberian, M. and King, G.C.P. Towards a paleogeography and tectonic evolution of 864 Iran. *Canadian Journal of Earth Sciences* **1981**, 18, 2010-2065. doi:10.1139/e81-019

Berberian, M. Master "blind" thrust faults hidden under the Zagros folds: active basement tectonics and surface morphotectonics. *Tectonophysics* **1995**, 241, 193-224. doi:10.1016/0040-1951(94)00185-C

Beydoun, Z. R., Hughes Clarke, M. W., Stonely, R. Petroleum in the Zagros Basin: A Late Tertiary Foreland Basin Overprinted onto the Outer Edge of a Vast Hydrocarbon-Rich Paleozoic-Mesozoic Passive-Margin Shelf: Chapter 11. In: Foreland Basin and Fold Belts. Macqueen, R. W. and Leckie, D. A. eds. *AAPG Special Volumes* **1992**, 55, 309-339. doi: 10.1306/M55563

Blanc, E. J.-P., Allen, M. B., Inger, S., Hassani, H. Structural styles in the Zagros Simple Folded Zone, Iran. *Journal of the Geological Society* **2003**, 160, 401-412. doi:10.1144/0016-764902-110

Byerlee, J. D. Frictional characteristics of granite under high confining pressure. *Journal of Geophysical Research* **1967**, 72, 3639-3648. doi: 10.1029/JZ072i014p03639

Byerlee, J. D. Friction of rocks. *PAGEOPH* **1978**, 116, 615-626. doi: 10.1007/BF00876528

Butler, R.W.H.; Mazzoli, S. Styles of continental contraction: A review and Introduction. In: Styles of Continental Contraction; Mazzoli, S., Butler, R.W.H., Eds.; *Geological Society of America: Boulder* **2006**, CO, USA. 414, 1-10. doi: 10.1130/2006.2414(01)

Candela, S.; Mazzoli, S.; Megna, A.; Santini, S. Finite element modelling of stress field perturbations and interseismic crustal deformation in the Val d'Agri region, southern Apennines, Italy. *Tectonophysics* **2015**, 657, 245-259. doi: 10.1016/j.tecto.2015.07.011

Carminati, E., Vadacca, L. Two- and three-dimensional numerical simulations of the stress field at the thrust front of the Northern Apennines, Italy. *Journal of Geophysical Research* **2010**, 115, B12425. doi: 10.1029/2010JB007870

Casciello, E., Vergés, J., Saura, E., Casini, G., Fernàndez, N., Blanc, E. J. P., Homke, S., Hunt, D. Fold patterns and multilayer rheology of the Lurestan Province, Zagros Simply Folded Belt (Iran). *Journal of the Geological Society of London* **2009**, 166, 974-59. doi:10.1144/0016-76492008-138

Colman-Saad, S. P. Fold development in Zagros simply folded belt, southwest Iran. *American Association of Petroleum Geologist Bulletin* **1978**, 62, 984-1003. doi:10.1306/C1EA4F81-16C9-11D7-8645000102C1865D

Copley, A. Postseismic afterslip 30 years after the 1978 Tabas-e-Golshan (Iran) earthquake: observations and implications for the geological evolution of thrust belts, *Geophysical Journal International* **2014**, 197, 665-679. doi:10.1093/gji/ggu023

Copley, A. and Reynolds, K. Imaging topographic growth by long-lived postseismic afterslip at Sefidabeh, east Iran, *Tectonics* **2014**, 33, 330-345. doi:10.1002/2013TC003462.

Csontos, L., Sasvári, Á., Pocsai, T., Kósa, L., Salae, A. T., and Ali, A. Structural evolution of the northwestern Zagros, Kurdistan Region, Iraq: Implications on oil migration. *GeoArabia* **2012**, 17(2), 81–116.

Dercourt, J., Zonenshain, L. P., Ricou, L. E., Kazmin, V. G., Le Pichon, X., Knipper, A. L., Grandjacquet, C., Sbortshikov, I. M., Geyssant, J., Lepvrier, C., et al. Geological evolution of the Tethys belt from the Atlantic to the Pamirs since the LIAS. *Tectonophysics* **1986**, 123, 914 241-315. doi:10.1016/0040-1951(86)90199-X

Dewey, J. W. and A. Grantz. The Ghir earthquake of April 10, 1972 in the Zagros Mountains of southern Iran: seismotectonic aspects and some results of a field reconnaissance. *Bulletin of the Seismological Society of America* **1973**, 63 (1973): 2071-2090.

DiBiase, R. A., Whipple, K. X., Heimsath, A. M., and Ouimet, W. B. Landscape form and millennial erosion rates in the San Gabriel Mountains, CA. *Earth and Planetary Science Letters* **2010**, 289(1-2), 134-144. doi: 10.1016/j.epsl.2009.10.036

Ellis, M.A., and Densmore, A. L. First-order topography over blind thrusts. In: Willett, S.D., Hovius, N., Brandon, M.T., and Fisher, D., eds., Tectonics, climate, and landscape evolution: *Geological Society of America Special Paper* **2006**, 398, Penrose Conference Series, p. 251-266, doi: 10.1130/2006.2398(15)

Emami, H., Vergès, J., Nalpas, T., Gillespie, P., Sharp, I., Karpuz, R., Blanc, E. J. P., Goodarzi,

M. G. H. Structure of the Mountain Front Flexure along the Anaran anticline in the Pusht-e Kuh Arc (NW Zagros, Iran): Insights from sand box models. *Geological Society of London Special Publication* **2010**, 330, 155-178. doi: 10.1144/SP330.9

Engdahl, E. R., Jackson, J. A., Myers, S. C., Bergman, E. A., and Priestley, K. Relocation and assessment of seismicity in the Iran region. *Geophysical Journal International* **2006**, 167, 761-78. doi: 10.1111/j.1365-246X.2006.03127.x

England, P., and Molnar, P. Surface uplift, uplift of rocks, and exhumation of rocks. *Geology* **1990**, 18, 1173-1177. doi: 10.1130/0091-7613(1990)018<1173:SUUORA>2.3.CO;2

Falcon, N. L. Major earth-flexuring in the Zagros Mountains of south-west Iran. *Quarterly Journal of the Geological Society of London* **1961**, 117, 367-76. doi:10.1144/gsjgs.117.1.0367

Falcon, N. L. Problems of the relationship between surface structure and deep displacements illustrated by the Zagros range. In: Time and Place Orogeny. Kent, P., Satterthwaite, G. and Spencer, A. eds. *Geological Society of London* **1969**, 9-22.

Feng, W., Samsonov, S., Almeida, R., Yassaghi, A., Li, J., Qiu, Q., Li, P., Zheng, W. Geodetic Constraints of the 2017 Mw7.3 Sarpol Zahab, Iran Earthquake, and Its Implications on the Structure and Mechanics of the Northwest Zagros Thrust-Fold Belt. *Geophysical Research Letters* **2018**, 45(14), 6853-6861. doi: 10.1029/2018GL078577

Florinsky, I. V. and Filippov, S. V. Three-dimensional desktop morphometric models for the Arctic Ocean floor. *International Cartographic Association*. Conference Proceedings. 29th International Cartographic Conference, Tokyo, Japan, 15-20 July **2019**. doi: 10.5194/ica-proc-2-32-2019

Förster, H.J.; Förster, A.; Oberhänsli, R.; Stromeyer, D. Lithospheric composition and thermal structure of the Arabian Shield in Jordan. *Tectonophysics* **2010**, 481, 29-37. doi: 10.1016/j.tecto.2008.11.014

Francois, T.; Burov, E.; Agard, P.; Meyer, B. Buildup of a dynamically supported orogenic plateau: Numerical modeling of the Zagros/Central Iran case study. *Geochemistry, Geophysics, Geosystems* **2014**, 15, 2632-2654. doi: 10.1002/2013GC005223

Gavillot, Y. G., Axen, G. J., Stockli, D. F., Horton, B. K., Fakhari, M. Timing of thrust activity in the High Zagros fold-thrust belt, Iran, from (U-Th)/He thermochronometry. *Tectonics* **2010**, 29, TC4025. doi:10.1029/2009TC002484

Ghasemi, A. and Talbot, C. J. A new tectonic scenario for the Sanandaj-Sirjan Zone (Iran). *Journal of Asian Earth Sciences* **2006**, 26, 683-693. doi:10.1016/j.jseaes.2005.01.003

Gombert, B., Duputel, Z., Shabani, E., Rivera, L., Jolivet, R., and Hollingsworth, J. Impulsive source of the 2017 Mw = 7.3 Ezgeleh, Iran, earthquake. *Geophysical Research Letters* **2019**, 46, 5207-5216. doi:10.1029/2018GL081794

Hessami, K., Koyi, H. A., Talbot, C. J., Tabasi, H., Shabanian, E. Progressive unconformities within an evolving foreland fold-thrust belt, Zagros Mountains. *Journal of the Geological Society of London* **2001**, 158, 969-981. doi:10.1144/0016-764901-007

Hessami, K., Nilforoushan, F., Talbot, C. J. Active deformation within the Zagros Mountain deduced from GPS measurements. *Journal of the Geological Society of London* **2006**, 163, 143-148. doi: 10.1144/0016-764905-031

Heydarizadeh Shali, H., Sampietro, D., Safari, A., Capponi, M., Bahroudi, A. Fast collocation for Moho estimation from GOCE gravity data: the Iran case study. *Geophysical Journal International* **2020**, 221(1), 651-664. doi: 10.1093/gji/ggaa026

Homke, S., Vergés, J., Garcés, M., Emami, H., Karpuz, R. Magnetostratigraphy of Miocene–Pliocene Zagros foreland deposits in the front of the Push-e Kush Arc (Lurestan Province, Iran). *Earth and Planetary Science Letters* **2004**, 225, 397-410. doi: 10.1016/j.epsl.2004.07.002

Jackson, J. Reactivation of basement faults and crustal shortening in orogenic belts. *Nature* **1980**, 283, 343–346. doi: 10.1038/283343a0

Jackson, J. and Fitch, T. Basement faulting and the focal depths of the larger earthquakes in the Zagros mountains (Iran). *Geophysical Journal of the Royal Astronomical Society* **1981**, 64, 561-586. doi:10.1111/j.1365-246X.1981.tb02685.x

Jassim, S. Z. and Goff, J. G. Geology of Iraq. 1st Edition **2006** *Prague and Moravian Museum, Brno, Czech Republic*.

Jiménez-Munt, I.; Fernàndez, M.; Saura, E.; Vergés, J.; Garcia-Castellanos, D. 3-D lithospheric structure and regional/residual Bouguer anomalies in the Arabia–Eurasia collision (Iran). *Geophysical Journal International* **2012**, 190, 1311–1324. doi: 10.1111/j.1365-246X.2012.05580.x

Kargaran, F.; Neubauer, F. Lithospheric thinning associated with formation of a metamorphic core complex and subsequent formation of the Iranian plateau. *GSA Today* **2015**, 25, 4-8. doi: 10.1130/GSATG229A.1

Koshnaw, R. I., Horton, B. K., Stockli, D. F., Barber, D. E., Tamar-Agha, M. Y., and Kendall, J. J. Neogene shortening and exhumation of the Zagros fold-thrust belt and foreland basin in the Kurdistan region of northern Iraq. *Tectonophysics* **2017**, 694, 332–355. doi: 10.1016/j.tecto.2016.11.016

Le Grazic, E., Vergés, J., Sapin, F., Saura, E., Meresse, F., Ringenbach, J. C. Evolution of the NW Zagros Fold-and-Thrust Belt in Kurdistan region of Iraq from balanced and restored crustal-scale sections and forward modeling. *Journal of Structural Geology* **2019**, 124, 51-69. doi:10.1016/j.jsg.2019.04.006

Leterrier, J. Mineralogical, Geochemical and isotopic evolution of two Miocene mafic intrusions from the Zagros (Iran). *Lithos* **1985**, 18, 311-29. doi:10.1016/0024-4937(85)90034-9

Liu, C., Zhu, B.J., Yang, X.L., Shi, Y.L. Crustal rheology control on earthquake activity across the eastern margin of the Tibetan Plateau: insignts from numerical modelling. *Journal of Asian Earth Sciences* **2015**, 100, 20-30. doi:10.1038/ncomms15992

Massaro, L., Corradetti, A., Tramparulo F. D. A., Vitale, S., Prinzi, E. P., Iannace, A., Parente, M., Invernizzi, C., Morsalnejad, D. and Mazzoli, S. Discrete Fracture Network Modelling in Triassic–Jurassic Carbonates of NW Lurestan, Zagros Fold-and-Thrust Belt, Iran. *Geosciences* **2019**, 9, 496. doi:10.3390/geosciences9120496

Megna, A., Barba, S., Santini, S. Normal-fault stress and displacement through finite element analysis. *Annals of Geophysics* **2005**, 48(6). doi:10.4401/ag-3250

Megna, A., Barba, S., Santini, S., Dragoni, M. Effects of geological complexities on coseismic displacement: hints from 2D numerical modelling. *Terra Nova* **2008**, 20, 173-179. doi: 10.1111/j.1365-3121.2008.00800.x

Megna, A.; Candela, S.; Mazzoli, S.; Santini, S. An analytical model for the geotherm in the Basilicata oil fields area (southern Italy). *Italian Journal of Geosciences* **2014**, 133, 204-213. doi: 10.3301/IJG.2014.02

Molnar, P.; Chen,W.P.; Padovani, E. Calculated temperatures in overthrust terrains and possible combinations of heat sources responsible for the tertiary granites in the greater Himalaya. *Journal of Geophysical Research* **1983**, 88, 6415–6429. doi: 10.1029/JB088iB08p06415

Mouthereau, F., Lacombe, O., and Vergés, J. Building the Zagros collisional orogen: Timing, strain distribution and the dynamics of Arabia/Eurasia plate convergence. *Tectonophysics* **2012**, 532, 27-60. doi:10.1016/j.tecto.2012.01.022

Motiei, H. Stratigraphy of Zagros. *Geological Survey of Iran Publication, Tehran* **1993**. 536.

Movaghari, R. and Javan Doloei, G. 3-D crustal structure of the Iran plateau using phase velocity ambient noise tomography. *Geophysical Journal International* **2019**, 220, 1555-1568. doi: 10.1093/gji/ggz537

Nissen, E., Tatar, M., Jackson, J. A., Allen, M. B. New views on earthquake faulting in the Zagros fold-and-thrust belt of Iran. *Geophysical Journal International* **2011**, 186(3), 928-944. doi:10.1111/j.1365-246X.2011.05119.x

Nissen, E., Ghods, A., Karasözen, A., Elliott, J. R. Barnhart, W. D. Bergman, E. A., et al. The 12 November 2017 Mw 7.3 Ezgeleh-Sarpolzahab (Iran) earthquake and active tectonics of the Lurestan arc. *Journal of Geophysical Research: Solid Earth* **2019**, 124, 2124-2152. doi:10.1029/2018JB016221

Paul, A., Kaviani, A., Hatzfeld, D., Vergne, J. and Mokhtari, M. Seismological evidence for crustal-scale thrusting in the Zagros mountain belt (Iran). *Geophysical Journal International* **2006**, 166, 227-237. doi: 10.1111/j.1365-246X.2006.02920.x

Paul, A., Hatzfeld, D., Kaviani, A., Tatar, M., & Péquegnat, C. Seismic imaging of the lithospheric structure of the Zagros mountain belt (Iran). *Journal of the Geological Society of London Special Publication* **2010**, 330, 5-18. doi: 10.1144/SP330.2

Pérez-Peña, J.V., Al-Awabdeh, M., Azañón, J.M., Galve, J.P., Booth-Rea, G., Notti, D. SwathProfiler and NProfiler: Two new ArcGIS Add-ins for the automatic extraction of swath and normalized river profiles. *Computers & Geosciences* **2017**, 104, 135-150. doi: 10.1016/j.cageo.2016.08.008

Pratt, B. R. and Smewing, J. D. Early Cretaceous Platform-Margin Configuration and Evolution in the Central Oman Mountains, Arabian Penisula. *The American Association of Petroleum Geologists* **1990**, 77, 225-244.

Ramezani, J. Regional geology, geochronology and geochemistry of the igneous and metamorphic rock suites of the Saghand area, central Iran. Ph.D. Thesis – *Washington University* **1997**.

Ramezani, J. and Tucker, R. D. The Saghand region, Central Iran: U-Pb geochronology, petrogenesis and implications for Gondwana Tectonics. *American Journal of Science* **2003**, 303(7), 622-665. doi: 10.2475/ajs.303.7.622

Sadeghi, S. and Yassaghi, A. Spatial evolution of Zagros collision zone in Kurdistan, NW Iran: constraints on Arabia-Eurasia oblique convergence. *Journal of Geophysical Research: Solid Earth* **2016**, 7, 659-672. doi:10.5194/se-7-659-2016

Santini, S., Basilici, M., Invernizzi, C., Mazzoli, S., Megna, A., Pierantoni, P. P., Spina, V., Teloni, S. Thermal Structure of the northern outer Albanides and adjacent Adriatic crustal sector, and implications for geothermal energy systems. *Energies* **2020**, 13(22), 6028. doi: 10.3390/en13226028

Schettino, A. and Scotese, C. Global kinematic constraints to the tectonic history of the Mediterranean region and surrounding areas during the Jurassic and Cretaceous. *Journal of the Virtual Explorer* **2002**, 7, 147-166.

Schütz, F.; Förster, H.J.; Förster, A. Thermal conditions of the central Sinai Microplate inferred from new surface heat-flow values and continuous borehole temperature logging in central and southern Israel. *Journal of Geodynamics* **2014**, 76, 8-24. doi: 10.1016/j.jog.2014.02.010

Searle, M. P., Warren, C. J., Waters, D. J., Parrish, R. R. Structural evolution, metamorphism and restoration of the Arabian continental margin, Saih Hatat region, Oman Mountains. *Journal of Structural Geology* **2004**, 26, 451-473. doi: 10.1016/j.jsg.2003.08.005

Sepehr, M. and Cosgrove, J. W. Structural framework of the Zagros Fold–Thrust Belt, Iran. *Marine and Petroleum Geology* **2004**, 21, 829-43. doi: 10.1016/j.marpetgeo.2003.07.006

Sharland, P. R., Archer, R., Casey, D. M., Hall, S. H., Heward, A. P., Horbury, A. D. and Simmons, M. D. Arabian Plate sequence stratigraphy. *Geo Arabia* **2001**, *special publication 2, Gulf Petrolink, Bahrain.*

Shekarifard, A.; Baudin, F.; Seyed-Emami, K.; Schnyder, J.; Laggoun-Défarge, F.; Riboulleau, A.; Brunet, M.F.; Shahidi, A. Thermal maturity of the Upper Triassic-Middle Jurassic Shemshak Group (Alborz Range, Northern Iran) based on organic petrography, geochemistry and basin modelling: Implications for source rock evaluation and petroleum exploration. *Geological Magazine* **2012**, 149, 19-38. doi: 10.1017/S0016756811000161

Sherkati, S., Letouzey, J., Frizon de Lamotte, D. Central Zagros fold-thrust belt (Iran): New insights from seismic data, field observation, and sandbox modeling. *Tectonics* **2006**, 25, TC4007. doi: 10.1029/2004TC001766

Sibson, R.H. Frictional constraints on thrust, wrench and normal faults. *Nature* **1974**, 249, 542-544. doi: 10.1038/249542a0

Stampfli, G. M. and Borel, G., D. A plate tectonic model for the Paleozoic and Mesozoic constrained by dynamic plate boundaries and restored synthetic oceanic isochrons. *Earth and Planetary Science Letters* **2002**, 196, 17-33. doi:10.1016/S0012-821X(01)00588-X

Stocklin, J. Structural History and Tectonic of Iran: A Review. *American Association of Petroleum Geologists Bulletin* **1968**, 52, 1229-1258. doi:10.1306/5D25C4A5-16C1-11D7-8645000102C1865D

Talbot, C. J. and Alavi, M. The past of a future syntaxis across the Zagros. *Geological Society of London Special Publications* **1996**, 100, 89-109. doi: 10.1144/GSL.SP.1996.100.01.08

Talebian, M. and Jackson, J. Offset on the Main Recent Fault of NW Iran and implications for the late Cenozoic tectonics of the Arabia–Eurasia collision zone. *Geophysical Journal International* **2002**, 157, 381-398. doi:10.1046/j.1365-246X.2002.01711.x

Talebian, M. and Jackson, J. A reappraisal of earthquake focal mechanisms and active shortening in the Zagros mountains of Iran, *Geophysical Journal International* **2004**, 156, 506–526, doi: 10.1111/j.1365-246X.2004.02092.x, 2004.

Tavani, S., Parente, M., Puzone, F., Corradetti, A., Gharabeigli, G., Valinejad, M., Morsalnejad, D., Mazzoli, S. The seismogenic fault system of the 2017 Mw 7.3 Iran-Iraq earthquake: constraints from surface and subsurface data, cross-section balancing, and restoration. *Journal of Geophysical Research: Solid Earth* **2018a**, 9, 821-831. doi:10.5194/se-9-821-2018

Tavani, S., Corradetti, A., Sabbatino, M., Morsalnejad, D., Mazzoli, S. The Meso-Cenozoic fracture pattern of the Lurestan region, Iran: the role of rifting, convergence, and differential compaction in the development of pre-orogenic oblique fractures in the Zagros Belt. *Tectonophysics* **2018b**, 749, 104-119. doi:10.1016/j.tecto.2018.10.031

Tavani, S., Camanni, G., Nappo, M., Snidero, M., Ascione, A., Valente, E., Gharabeigli, G., Morsalnejad, D., Mazzoli, S. The Mountain Front Flexure in the Lurestan region of the Zagros belt: Crustal architecture and role of structural inheritances. *Journal of Structural Geology* **2020**, 135, 104022. doi:10.1016/j.jsg.2020.104022

Teknik, V. and Ghods, A. Depth of magnetic basement in Iran based on fractal spectral analysis of aeromagnetic data. *Geophysical Journal International* **2017**, 209, 1878-1891. doi: 10.1093/gji/ggx132

Teknik, V.; Ghods, A.; Thybo, H.; Artemieva, I.M. Crustal density structure of the northwestern Iranian Plateau. *Canadian Journal of Earth Sciences* **2019**, 56, 1347-1365. doi: 10.1139/cjes-2018-0232

Tunini, L.; Jiménez-Munt, I.; Fernàndez, M.; Vergés, J.; Villaseñor, A. Lithospheric mantle heterogeneities beneath the Zagros Mountains and the Iranian Plateau: A petrological-geophysical study. *Geophysical Journal International* **2015**, 200, 596–614. doi: 10.1093/gji/ggu418

Vajedian, S., Motagh, M., Mousavi, Z., Motaghi, K., Fielding, E. J., Akbari, B., Wetzel, H. U., Darabi, A. Coseismic Deformation Field of the Mw 7.3 12 November 2017 Sarpol-eZahab (Iran) Earthquake: A Decopuling Horizon in the Northern Zagros Mountains Inferred from InSAR Observations. *Remote Sensing* **2018**, 10, 1589. doi: 10.3390/rs10101589

Vergés, J., Emami, H., Homke, S. and Garcés, M. Neogene Sequence of Folding in the NW Zagros Fold Belt Dating Non-marine Foreland Growth Strata. *European Association of Geoscientists & Engineers*. Conference Proceedings. 1st EAGE International Petroleum Conference and Exhibition, Shiraz, May **2009**. doi: 10.3997/2214-4609.20145863

Vergés, J., Saura, E., Casciello, E., Fernàndez, M., Villaseñor, A., Jiménez-Munt, I., García-Castellanos, D. Crustal-scale cross-sections across the NW Zagros belt: implications for the Arabian margin reconstruction. *Geological Magazine* **2011a**, 148, 739-761. doi:10.1017/S0016756811000331

Vergés, J., Goodarzi, M. G. H., Emami, H., Karpuz, R., Efstathiuou, J., Gillespie, P. Multiple Detachment Folding in Pusht-e Kuh Arc, Zagros: Role of Mechanical Stratigraphy. In: Thrust fault-related folding. McClay, K., Shaw, J. H. and Suppe, J. eds. *AAPG Memoir* **2011b**, 94, 69-94. doi: 10.1306/13251333M942899

Vernant, P., Nilforoushan, F., Hatzfeld, D., Abassi, M., Vigny, C., Masson, F., Nankali, H., Martinod, J., Ashtiani, A., Bayer, R., Tavakoli, F., Chery, J. Contemporary Crustal Deformation and Plate Kinematics in Middle East constrained by GPS Measurements in Iran and North Oman. *Geophysical Journal International* **2004**, 157(1), 381-398. doi:10.1111/j.1365-246X.2004.02222.x

Vernant, P. and Chéry, J. Mechanical modelling of oblique convergence in the Zagros, Iran. *Geophysical Journal International* **2006**, 165, 991-1002. doi:10.1111/j.1365-246X.2006.02900.x

Vigny, C., Rudloff, A., Ruegg, J.C., Madariaga, R., Campos, J., Alvarez, M. Upper plate deformation measured by GPS in the Coquimbo gap, Chile. *Physics of the Earth and Planetary Interiors* **2009**, 175, 86-95. doi:10.1016/j.pepi.2008.02.013

Wang, Z., Zhang, R., Wang, X., Liu, G. Retrieving Three-Dimensional Co-Seismic Deformation of the 2017 Mw7.3 Iraq Earthquake by Multi-Sensor SAR images. *Remote Sensing* **2018**, 10, 857. doi:10.3390/rs10060857

Warburton, J., Burnhill, T. J., Graham, R. H., Isaac, K. P., Robertson, A. H. F., Searle, M. P., Ries, A. C. The evolution of the Oman Mountains foreland basin. *Journal of the Geological Society of London Special Publication* **1990**, 49, 419-427. doi:10.1144/GSL.SP.1992.049.01.26

Whipple, K. X. Fluvial landscape response time: how plausible is steady-state denudation? *American Journal of Science* **2001**, 301, 313-325. doi: 10.2475/ajs.301.4-5.313

Williams, C. A. and Richardson R. M. A rheological layered three-dimensional model of the San Andreas Fault in central and southern California. *Journal of Geophysical Research: Solid Earth* **1991**, 96, 16, 597-623. doi:10.1029/91JB01484

Zhao, S., Műller, R. D., Takahashi, Y., Kaneda, Y. 3-D finite-element modelling of deformation and stress associated with faulting: effect of inhomogeneous crustal structures. *Geophysical Journal International* **2004**, 157, 629-644. doi: 10.1111/j.1365-246X.2004.02200.x

Zhuang, Z., Liu, Z., & Cui, Y. Equivalent Stress and Equivalent Strain. In: Dislocation Mechanism-Based Crystal Plasticity, Par. 3.2.6, 67-69, *Academic Press Book – Elsevier* **2019**. doi: 10.1016/C2017-0-01936-5

Zun, S., Zhang, P. FEM simulation of interseismic and coseismic deformation associated with the 2008 Wenchuan Earthquake. *Tectonophysics* **2013**, 584, 64-80. doi: 10.1016/j.tecto.2012.06.024

Acknowledgments

I would like to offer my sincere thanks to supervisors Prof. Stefano Santini and Prof. Stefano Mazzoli. I am particularly pleased to them for giving me this study and work opportunity.

I thank the co-supervisor Ph.D. Antonella Megna for following my work with patience, great expertise and meticulous attention to detail.

I thank all collaborators from University of Naples “Federico II”: Prof. Stefano Tavani, Prof.ssa Alessandra Ascione and Ph.D. Ettore Valente; from University of Camerino: Prof. Pietro Paolo Pierantoni and Ph.D. student Simone Teloni; and from Total Upstream Denmark: Ph.D. Vincenzo Spina.

I thank the reviewers Prof.ssa Chiara Invernizzi and Prof. Domenico Liotta for their useful comments and suggestions.

At the end, I would like to express my gratitude to my family and my girlfriend for their support during the entire Ph.D. course.